HOMOGENISED MODELS OF SMOOTH MUSCLE AND ENDOTHELIAL CELLS

Jimmy Shek
Under the supervision of Prof. Tim David and Dr. Rua Murray.

A thesis presented for the degree of Masters in Bioengineering at the University of Canterbury, Christchurch, New Zealand.
December 9th 2013

Abstract

Numerous macroscale models of arteries have been developed, comprised of populations of discrete coupled Endothelial Cells (EC) and Smooth Muscle Cells (SMC) cells, an example of which is the model of Shaikh et al. (2012), which simulates the complex biochemical processes responsible for the observed propagating waves of Ca^{2+} observed in experiments. In a 'homogenised' model however, the length scale of each cell is assumed infinitely small while the population of cells are assumed infinitely large, so that the microscopic spatial dynamics of individual cells are unaccounted for.

We wish to show in our study, our hypothesis that the homogenised modelling approach for a particular system can be used to replicate observations of the discrete modelling approach for the same system. We may do this by deriving a homogenised model based on Goldbeter et al. (1990), the simplest possible physiological system, and comparing its results with those of the discrete Shaikh et al. (2012), which have already been validated with experimental findings. We will then analyse the mathematical dynamics of our homogenised model to gain a better understanding of how its system parameters influence the behaviour of its solutions. All our homogenised models are essentially formulated as partial differential equations (PDE), specifically they are of type reaction diffusion PDEs. Therefore before we begin developing the homogenised Goldbeter et al. (1990), we will first analyse the Brusselator PDE with the goal that it will help us to understand reaction diffusion systems better. The Brusselator is a suitable preliminary study as it shares two common properties with reaction diffusion equations: oscillatory solutions and a diffusion term.

Contents

Chapter 1

Introduction

Given a particular cell population system, we may develop a discrete computational model or a homogenised computational model to simulate the same system. We hypothesise that the two modelling approaches are just two different methods of arriving at the same outcome. A lot of discrete models have already been developed, the macroscale arterial system of $\sim 20,000$ discretely coupled Endothelial (EC) and Smooth Muscle Cells (SMC) of Shaikh et al. (2012) being one such example. The model exploits the computational capabilities of parallelism offered by the BlueGene/P supercomputers, and it simulates a linear arterial segment. But already the focus is now aimed at extending this model into $\sim 1million$ cells, and at implementing the arterial structure into the more physiologically realistic trifurcating geometry. In the future, it is hoped that such a trifurcating structure can be used as a building block, connecting other trifurcating structures to form a vast vascular network, and so the potential is limitless.

Our first aim in this thesis is to prove whether a homogenised system is able to replicate the behaviours of its discrete counterpart, and thus prove whether homogenisation can be used as an alternative approach to discrete modelling. One of the behaviours exhibited by a discrete coupled cell arterial model is that of an oscillating wave of calcium propagating along a population of cells: referred to as a 'travelling wave'. We will compare the physical properties of a travelling wave from a homogenised system, to a travelling wave produced from a discrete system in order to benchmark our newly developed homogenised model and thus prove our hypothesis. Once we have proven this, we may use homogenised models to learn about their corresponding discrete models. In particular, our second aim is to study the mathematical dynamics of our homogenised systems in order to gain more insight into their equivalent discrete systems. As with the development of discrete cell systems, there are varying levels of complexity for homogenised models, ranging from simple theoretical models to the considerably more complex and non-linear systems. In the scope of this thesis however, our focus shall only be on developing the more simpler homogenised equations which have fewer parameters, the reason being that we can understand how these parameters affect the behaviour of the system far better than we would by analysing a more complex system which has more parameters.

In homogenisation, denoting the number of cells to be n and the length scale of each cell l, we assume that in the limit $n \to \infty$ and $l \to 0$, $n \cdot l = constant$, such that we model the behaviour of a continuum population of cells. Mathematically our homogenised systems are a set of reaction-diffusion equations, with a 'Fickian' diffusion term incorporated into them, accounting for chemical spec ies diffusing across the continuum of cells. In our case, the travelling wave is a diffusion of calcium along a population of homogenised cells.

In a single cell, there is an intricate network of cell channels, pumps and storage organelles, all operating to create 'periodic peaks' in calcium concentration, what we refer to as calcium oscillations. When this calcium oscillation spreads to other neighbouring cells, it is a 'travelling wave'. There is a sequence of biochemical reactions that take place within a cell before oscillations can arise. As such, our model development involves implementing the ordinary differential equations (ODEs) that model this biochemical cascade.

But what is the underlying motivation behind our work on travelling waves? We can understand the bigger picture by considering that as early as 1969, Caro et al. (1969) hypothesized from their post mortem studies of bifurcating blood arteries, a relationship between disturbed flow and atherosclerotic plaque formation in arteries. In disturbed flow regions, there are a number of notable features. Firstly, impaired mass transfer of agonist species ATP occurs in this region, whereby species concentration is reduced and a thicker concentration boundary layer is observed (Ma et al., 1997). Secondly, low wall shear stress (WSS) is associated with disturbed flow. WSS has a profound effect on the cytoskeletal structure of ECs, the proliferation rate of ECs, and the calcium dynamics responsible for the ultimate relaxation of SMCs. It follows that calcium dynamics in the haemodynamic environments of disturbed flow are notably different from those in undisturbed flow. An understanding of the calcium ion responses within populations of ECs and SMCs in disturbed flow, may offer us more understanding in how the biochemistry of arterial cells can favour plaque formation. We can therefore provide the missing link in the hypothesis set out by Caro et al. (1969). The biochemical reasoning underlying the relationship hypothesized by Caro et al. (1969) has yet to be eludicated. So we hope that the numerically simulated models we develop will serve to explain how the biochemical mechanism due to disturbed flow can cause atheroma.

Chapter 2 begins with an explanation of the basic inner components of a cell, and how such components operate to generate calcium oscillations. When these oscillations propagate from cell to cell, it is known as a travelling wave. The chapter then explores the various different types of discrete computational cell models that have already been developed.

Chapter 3 is an explanation of how reaction diffusion equations (RD) are derived from 'Fickian' diffusion and the chapter also explores the various applications of RD systems in the field of mathematical biology. This is

important, as all homogenised cell models are formulated as reaction diffusion PDEs. The chapter also explains the numerical methodology behind the models we shall develop: in particular, the Brusselator, and Goldbeter based model.

Chapter 4 explains all the numerical results obtained from the Brusselator and Goldbeter model, but also the travelling wave analysis work we have carried out on the two systems in order to consolidate the numerical findings. We also performed a Turing instabilities analysis on the Brusslator system, where consistent with our numerical results, diffusion driven instabilities are shown to occur for certain parameter values.

Chapter 2

Literature Review

2.1 Anatomy and Physiology

In this section we explore the inner workings of a general eukaryotic cell, where there are a network of ion channels and pumps that operate to create calcium oscillations inside the cell. Figure(2.1) gives a summary of these organelles. These oscillatory signals can spread from cell to cell, and we refer to this as a 'travelling wave'. As these waves vary over space in a population of cells and they also vary with time progression, we will refer to these as 'spatio-time' patterns of calcium concentration. We are interested in the direct comparison of calcium spatio-temporal patterns produced from our homogenised models with patterns from discrete models that have already been developed, as this will provide us with a means of validating our newly developed homogenised models. In many types of cells, calcium acts as an important signalling molecule (Meyer and Stryer, 1991), where changes in the calcium in the cytosol of the cell are responsible for various cell functions: proliferation, secretion, metabolic adjustments to name just a few. Berridge (1993) But the most relevant function for our study is vasomotion: the periodic contraction and relaxation of the arterial vessel. A vascular smooth muscle cell (SMC) contracts when the calcium concentration within it increases, so it follows that a synchronised calcium increase in the population of smooth muscle cells making up the arterial vessel causes a constant vessel contraction. But it is only when the population of SMCs undergoes synchronised calcium oscillations do we observe vasomotion.

We will illustrate the biochemical pathway responsible for producing calcium oscillations using the simplest model that has been developed: the 'calcium induced calcium model' (CICR), formulated by Goldbeter et al. (1990). There are numerous models, far more advanced and complex than that of Goldbeter et al. (1990), and these systems are the most realistic. However they are all fundamentally based on Goldbeter et al. (1990), where the calcium induced calcium release mechanism is the main mechanism causing calcium oscillations. Table (2.2) shows the series of CICR models that have been developed. In the text that follows we will explore all the components within the cell, namely the ion channels and intracellular organelles, before attempting to understand the

CICR pathway. Although some of the components are not included in the simple Goldbeter et al. (1990) system, they are included in the more advanced ones that follow, and are thus worth mentioning.

Vasoconstrictors (agonists)
Vasoconstrictors are chemical molecules that bring about an ultimate contraction of the blood vessel. Vasoconstrictors are found in the blood flowing through the vessel, and as they attach to the receptors of cells lining the inner surface of the blood vessel, they initiate a biochemical pathway which results in an increase of intracellular calcium. An increase in calcium in the population of cells comprising the vessel causes the vessel to constrict. The term 'agonist' refers more generally to any molecule that binds to a cell receptor to initiate a response in that cell. Examples of vasoconstrictors are: Phenylephrine (PE), Potassium Chloride (KCl), Vasopressin, Norepinephrine (NE), Adenosine triphosphate (ATP)

Second Messenger Molecule: Inositol trisphosphate (IP_3) and Calcium (Ca^{2+})
When an agonist, say ATP attaches to a receptor on the surface of a cell, it initiates the production of Inositol trisphosphate (IP_3) inside the cell, and (IP_3) is free to move around the cytosol. (IP_3) then initiates the release of Ca^{2+} from internal stores inside the cell. This released Ca^{2+} initiates a mechanism (explained in figure (2.4) of section 2.2) which results in the generation of calcium oscillations. We therefore say that (IP_3) is a second messenger: the agonist essentially acts as a signal, signalling the release of Ca^{2+} inside the cell, but this is only possible via a secondary messenger ((IP_3)) that relays the agonist signal. Calcium itself is also a signalling molecule, it directly modulates a lot of cell behaviour, one of which is cell contraction. An increase in Ca^{2+} inside the cell causes it to contract, while oscillating Ca^{2+} inside the cell causes the cell to undergo cyclic contraction and relaxation. When these oscillations spread along a population of cells comprising a blood vessel, we get vasomotion: the periodic contraction and relaxation of the entire vessel. So Ca^{2+} can act as a signal, coordinating and propagating cell responses over large distances.

Ion Channels, Pumps and Transporters
The passage of almost all ions and molecules into and out of the cell is only possible through selective membrane transport proteins, and these proteins are classed into the 3 categories of ion channels, ion pumps and ion transporters. Table 2.1 summarises these ion pumps and channels.

Ion Channels: (includes
Small conductance Ca^{2+} activated K^+ channels (SK_{Ca}),
Large conductance Ca^{2+} activated K^+ channels (BK_{Ca}),
Voltage operated calcium channels (VOCCs))
Passage of ions and molecules through these channels is reliant on the electrical and concentration gradient across the membrane, where species travel from a high potential/concentration down to a low potential/concentration. These channels do not require any conformational protein change during ion/molecule passage and as such, they have relatively high transport rates,

Component name	Abbreviation	Type	Role
Cytosol			This is the space inside the cell. Ions and molecules are free to move around the cytosol.
Small/large conductance calcium activated potassium channel	$SK_{Ca,}$ BK_{Ca}	Ion channel	Brings about efflux of potassium out of cell. Activates when calcium attaches to it. Efflux of calcium hyperpolarises the cell.
Voltage operated calcium channel	VOCC	Ion channel	Allows influx of calcium into cell. Activates when the cell is depolarised but de-activates when cell is hyperpolarised. Influx of calcium depolarises the cell further.
SERCA pump	Ca2+-ATPase or SERCA pump	Ion pump	Pumps calcium back into the ER/SR store, thereby replenishing it.
Sodium-calcium antiporter	Na2+/Ca2+ antiporter	Ion transporter	
Endoplasmic/ sarcoplasmic reticulum	ER/SR	Ion store	This organelle is found inside the cell and acts as an 'internal store' for calcium. It both releases and pumps calcium back from the cytosol. This cycling of calcium in and out of ER/SR forms the fundamental mechanism for calcium oscillations.
Gap junction			Channels that connect the cells together. Allows passage of molecules (calcium and IP3) between cells.

Definition of terminology
Hyperpolarisation: a state of the cell in which it is negatively charged.
Depolarisation: a state of the cell in which it is positively charged.

Figure 2.1: Table summarises the various ion channels, ion pumps and organelles responsible for generating calcium oscillations within a cell. The inclusion of certain cell components in a computational model is dependent on the complexity and physiological reelevence of that particular model. For example, voltage operated calcium channels (VOCCs) and potassium channels (SK_{Ca}) are present in Shaikh et al. (2012) but are not present in the minimal Goldbeter et al. (1990) model.

Figure 2.2: Table summarises the main calcium induced calcium release mechanism (CICR) based models that have been developed. Arrows indicate how the more complex models are based on the simpler models. As shown, the most complex system by comparison to the other models in the table is Shaikh et al. (2012) and the simplest is Goldbeter et al. (1990).

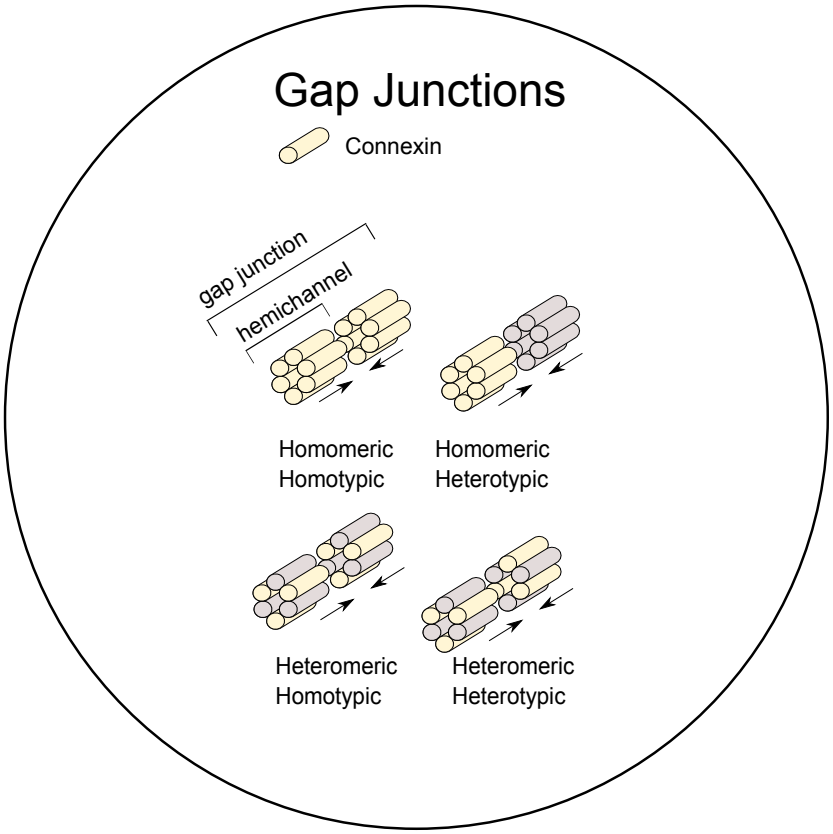

Figure 2.3: Diagram illustrates the composition of gap junctions. Two hemichannels combine to form a gap junction. A hemichannel comprises of 6 connexin proteins. A heteromeric hemichannel is one which is formed from different connexins, but a homomeric is one formed from the same connexins. A homotypic gap junction is where all 12 connexins of the 2 hemichannels are of the same type, but a heterotypic gap junction is where each hemichannel is homomeric and of different connexin isoform.

$\sim 10^8$ ions/s Lodish et al. (2008), compared to ion pumps/transporters.
SK_{Ca} and BK_{Ca} channels activate (open up) when calcium molecules attach to it, thus allowing potassium molecules out of the cell. This hyperpolarises the cell.
VOCCs activate whenever the inside of the cell is depolarised, but close whenever the cell is hyperpolarised. When VOCCs open, there is an influx of calcium into the cell.

Ion Pumps: (include $Ca^{2+} - ATPase$ pumps (SERCA pumps)
Ion pumps utilise the energy released from ATP hydrolysis for the pumping of ions/molecules against an often high concentration/potential gradient (active transport). In the case of $Ca^{2+} - ATPase$ (SERCA), these pumps transport Ca^{2+} (from cytosol to ER/SR) against a concentration difference of 3 to 4 magnitude, since cytosolic $[Ca^{2+}]$ is typically of $\sim 0.1\mu M$ while ER/SR $[Ca^{2+}]$ can be as high as 1mM. (Fall, 2002). $Ca^{2+} - ATPase$ increases its activity when cytosolic $[Ca^{2+}]$ rises, and its role is to maintain ER/SR Ca^{2+} stores (Fall, 2002) and also, with the aid of membrane pumps, ensure that cytosolic $[Ca^{2+}]$ does not exceed $1\mu M$. Typical of ATP-pumps, the protein undergoes conformational change during ion/molucule transport, thus accounting for the relatively slow transport rate.

Ion Transporters: (include Na^+/Ca^{2+} antiporter)transporter proteins may be further categorised into the two general classes: uniporters and cotransporters. Analogously to ion pumps, cotransporters utilise the energy released from ions/molecules moving down a concentration gradient to actively transport other ions/molecules against their concentration gradient. As suggested by their name, uniporters only transports a single species of ion/molecule by facilitated diffusion.

Mitochondria
Amongst the many important roles of the Mitochondria, generation of ATP by oxidative phosphorylation is one of them. (Carroll, 1989). But in the context of our study, these organelles play a vital role in the generation of cytosolic Ca^{2+} oscillations in the $IP_3 - Ca^{2+}$ cross-coupling model of Meyer and Stryer (1988). Refer to (section 2.3.2). In the *deactivation* step, the mitochondrion sequesters cytosolic Ca^{2+} ions through the Ca^{2+} uniporter when cytosolic Ca^{2+} reaches a threshold level.

Endoplasmic Reticulum/Sarcoplasmic Reticulum
The endoplasmic reticulum resides in the endothelial cell, while sarcoplasmic reticulum are found in the smooth muscle cell. In the SMC, the SR has a disproportionately high Ca^{2+} concentration (as high as $10^{-2}M$) compared to free cytosolic Ca^{2+} concentration (ranging from $10^{-7}M$ in resting cells to 10^{-6} during cell contraction). (Lodish et al., 2008). So from the perspective of our study, SR mainly acts as a Ca^{2+} store, with the aid of $Ca^{2+} - ATPase$ and a calcium leak channel in maintaining this store.

Gap Junctions
Gap junctions are channels that connect individual cells together to form a network of interconnected cells that make up a whole blood vessel. Refer to

diagram (2.3) for a graphical illustration of gap junctions. Gap junctions allow the passage of ions and molecules between cells, essentially allowing cells to communicate with each other. The importance of gap junctions can be appreciated when we consider that vascular networks constrict and dilate in a co-ordinated manner.

A hemichannel (connexon) comprises of 6 connexin proteins, and a functional gap junction comprises of 2 hemichannels 'docked' together, (one hemichannel from each neighbouring cell). A heteromeric hemichannel is one which is formed from diffrent connexins, wheras a homomeric hemichannel is a collection of connexins of the same type. (Haefliger et al., 2004).

A gap junction can be homotypic: where all 12 connexins of the 2 hemichannels are of the same type, or it may be heterotypic: where each hemichannel is homomeric and of different connexin isoform. (Rackauskas et al., 2007a). Further, a heterocellular gap junction is the junction formed between two different types of cells (for instance, between an EC and an SMC (EC-SMC or SMC-EC)), while a homocellular junction arises from the coupling of two cells of the same type (for example, SMC-SMC or EC-EC). In the case of smooth muscle and endothelial cells, heterocellular junctions (or myoendothelial junctions) allow for transverse signal propagation, that is, the propagation direction is perpendicular to the longitudinal axis of the vessel, while homocellular junctions (EC-EC or SMC-SMC) allow longitudianal signal propagation.

There are 19 connexin isoforms (Diep et al., 2005), of these, the 3 most commonly expressed isoforms in vasculature are $C \times 37, C \times 40 and C \times 43$ (Arensbak et al., 2001), but the expression varies according to species, vascular bed, and pathological state of vasculature. (Hill et al., 2001).

$C \times 40$ connexins are the most abundant connexin found in ECs (van Kempen and Jongsma, 1999), and in general, in tissues with undisturbed flow (Shaikh et al., 2012). They are rarely found in SMCs, but of the few instances when they are observed in SMCs, they are only found in small arteries/arterioles. (Physiol et al., 2013).

$C \times 37$ connexins are expressed in most small arteries and arterioles ECs (Shaikh et al., 2012), and in general in tissues in undisturbed flow.

$C \times 43$ connexins in ECs are site specific, and are often reported in disturbed flow areas (arterial bifurcations and branch points) (Dai et al., 2004) and in pathological tissues. In SMCs, they are commonly observed in muscular arteries (Arensbak et al., 2001).

2.2 What causes calcium Ca^{2+} Oscillations

Now that we have understood the inner components of the cell, and their functions, we can begin to understand the biochemical mechanism behind

intracellular calcium Ca^{2+} oscillations, and we will use the model of Goldbeter et al. (1990) to do this. It is the simplest model that has been developed, from which successively more sophisticated and realistic models are based on. Refer to figure (2.4).

Following agonist stimulation, the chemical cascade responsible for Ca^{2+} oscillations is:

1. Agonist attaches to a cell surface receptor (R), and activates a G protein (Gp). Phospholipase C (PLC) also activates. PLC catalyses the the hydrolysis of PIP_2 to IP_3 and diacylglycerol (DG). IP_3 is released into cytosol at this point.

2. Cytosolic IP_3 attaches to receptors on IP_3 sensitive pool, and Ca^{2+} is released into the cytosol from this pool.

3. Cytosolic Ca^{2+} activates ryodine receptors on the Ca^{2+}-sensitive pool to release yet more Ca^{2+} into the cytosol. A large peak in cytosolic Ca^{2+} can thus be observed.

4. Following the peak in cytosolic Ca^{2+}, $Ca^{2+} - ATPase$ pump on the Ca^{2+} sensitive store begins the re-uptake of cytosolic Ca^{2+} back into the store. Extracellular influx of Ca^{2+} into cytosol also contributes to this replenishment. A passive Ca^{2+} leak from this store into the cytosol is also accounted for in the model.

5. All the while there is a constant influx of extracellular Ca^{2+} into cytosol (removal of which eventually suppresses Ca^{2+} oscillations), and a linear efflux of Ca^{2+} from cytosol to extracellular space.

So we can see that cytosolic calcium (Ca^{2+}) oscillations arise from the cycling of calcium into and out of the calcium sensitive store. Further, cytosolic Ca^{2+} can spread to neighbouring cells (which are in a non-oscillatory state) through gap junctions to induce oscillations in these cells. As illustrated above, this is achieved through activation of receptors by Ca^{2+} in Ca^{2+}-sensitive pool.

2.3 Computational Cell Models

(Figure 2.2 gives a summary of the various CICR models that have been developed. We are primarily interested in the CICR in this thesis). Now that we have understood the model of Goldbeter et al. (1990), it is worth exploring that of Shaikh et al. (2012). It is fundamentally based on the CICR mechanism of Goldbeter et al. (1990) for producing oscillations, but Shaikh et al. (2012) has an additional 'membrane oscillator' mechanism incorporated into it. This is a set of additional ion channels causing the electrical membrane potential of the cell to oscillate. Of course, Shaikh et al. (2012) is a far more complex system, such that developing a 'homogenised' version of it would not offer us much more understanding of the nonlinear dynamics of the system than what we already know from the original discrete version. Instead, since Shaikh et al. (2012) is based on Goldbeter et al. (1990), we will analyse in considerable detail the parameters of homogenised Goldbeter et al. (1990) and

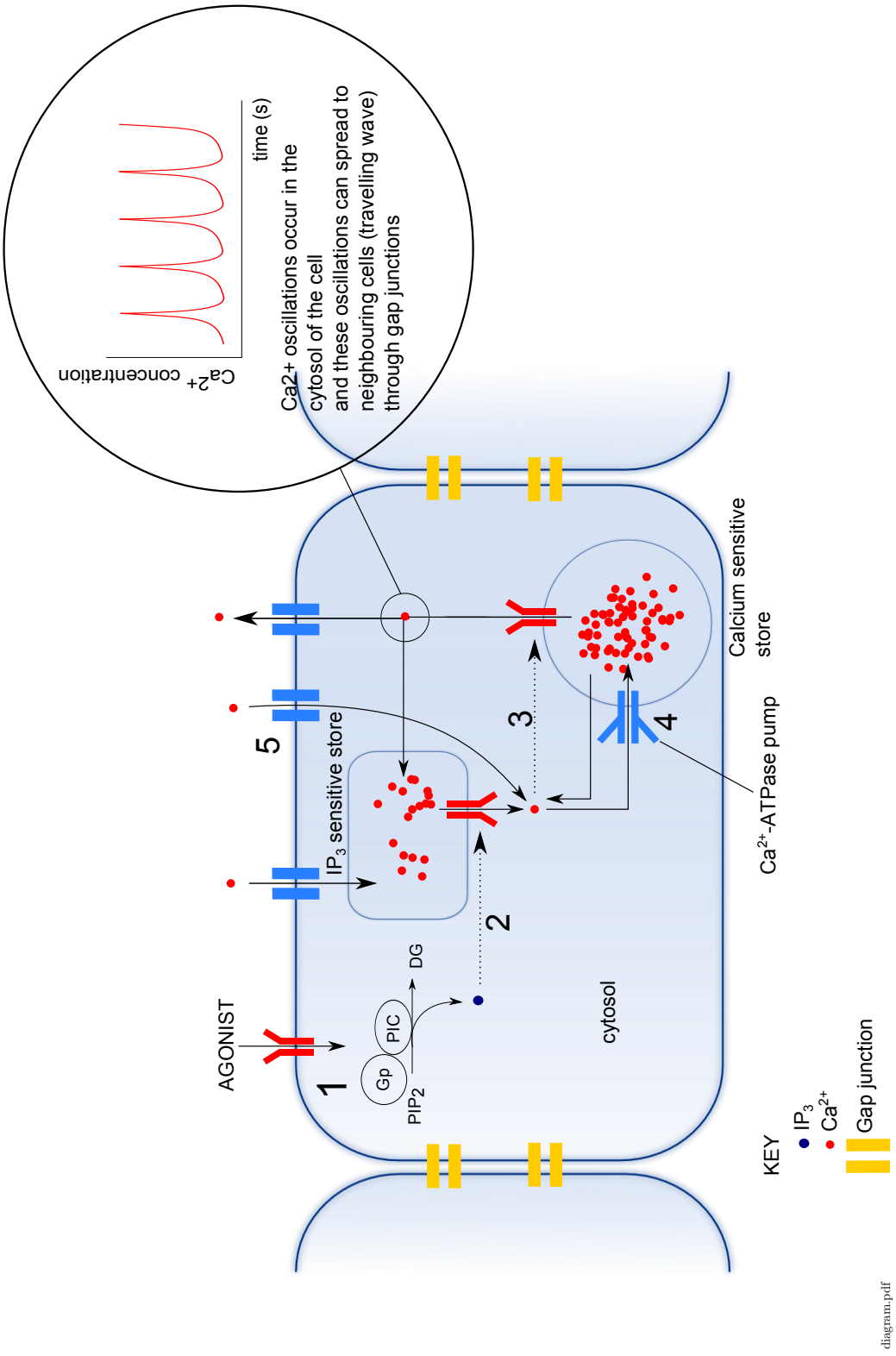

Figure 2.4: Diagram shows the cascade of biochemical steps responsible for generating calcium oscillations. This is the minimal CICR based model of Goldbeter et al. (1990), and we will be developing the homogenised form of this in our work. Diagram created using Inkscape. Jimmy Shek. Homogenised Models of SMCs and ECs. 2013

this should help us to elucidate the nonlinear dynamics of the discrete model of Shaikh et al. (2012). In this section we will also explore other models, that use different mechanisms to that of Goldbeter et al. (1990) and Shaikh et al. (2012)

In general, calcium oscillation models may be classed into 3 categories, corresponding to the 3 different mechanisms responsible for generating oscillations:

1. Calcium Induced Calcium Release (CICR) based models. The class of models where Ca^{2+} oscillations can occur even without IP_3 oscillations. Includes: Shaikh et al. (2012) and Goldbeter et al. (1990)

2. $IP_3 - Ca^{2+}$ Cross Coupling (ICC) based models. The class of models requiring IP_3 oscillations for Ca^{2+} oscillations to take place. Includes Meyer and Stryer (1988)

3. Biphasic based models. Models in which Ca^{2+} release from intracellular ER stores are inhibited by low and high levels of cytosolic Ca^{2+}, while only intermediate Ca^{2+} levels allow for release.

Note that this is only a broad categorisation, as there are many models that incorporate different types of mechanisms into their systems.

2.3.1 Calcium Induced Calcium Release (CICR) based models.

(Figure 2.2 gives a summary of the various CICR models that have been developed. We are primarily interested only in the CICR models in this thesis).

The simplest CICR system is that of Goldbeter et al. (1990), a minimal model with only sufficient components to generate Ca^{2+} oscillations, namely SERCA uptake and CICR release. It does not account for the ion channels responsible for membrane oscillator, but the model forms the basis for more complex systems that follow. In the single cell model of Parthimos et al. (1999), the CICR oscillator is coupled non-linearly to the membrane oscillator, giving considerably more complex dynamics. The Koenigsberger et al. (2004) system is a development of Parthimos et al. (1999), and consists of a 2 dimensional discrete coupled cell monolayer of SMCs, to investigate the effects of Ca^{2+}, IP_3 and membrane potential (V) coupling on Ca^{2+} oscillations. It was shown that membrane oscillations alone could generate asynchronous Ca^{2+} oscillations in neighbouring cells, but the membrane oscillations were synchronous. When only IP_3 coupling was allowed, IP_3 oscillations were observed to be capable of synchronising Ca^{2+} oscillations, although this effect was limited, owing to the small amplitude of IP_3 oscillations, which causes IP_3 and Ca^{2+} oscillations to be weakly coupled. In Koenigsberger et al. (2005), an additional EC layer was coupled to the SMC monolayer of Koenigsberger et al. (2004), and the endothelial layer was demonstrated to have an important modulatory effect on the Ca^{2+} oscillations of the underlying SMC layer, although SMCs do not require ECs for oscillations to occur. The major effect of the endothelium is to bring about an SMC Ca^{2+} decrease, caused by two

processes incorporated into their EC system: the NO pathway and the opening of SK_{Ca} channels. For SMCs initially with Ca^{2+} oscillations (induced by a fixed agonist concentration), the introduction of endothelial effects abolishes these oscillations, however the opposite is true for SMCs intially in a steady state, as introducing endothelial effects induces Ca^{2+} oscillations. So the authors have shown that depending on the initial state of SMCs, the endothelium can either induce or abolish SMC calcium oscillations.

Koenigsberger et al. (2010)
In the laboratory work of Koenigsberger et al. (2010) on endothelium denuded rat mesenteric strips, inserting the arterial strip in an extracellular Ca^{2+} free solution prevented Ca^{2+} wave propagation when a local $40\mu m$ PE stimulation was applied. This highlights the importance of extracellular calcium in wave propagation. Further, the $40\mu m$ local PE stimulation only generated propagating Ca^{2+} waves when the global concentration for the arterial strip was at a baseline of PE=$0.3\mu m$. At a global PE=$0\mu m$ however, only a local Ca^{2+} rise resulted from the $40\mu m$ local stimulation. The authors also highlighted the importance of VOOCs in wave propagation, as the addition of Nifedipine (a blocker of VOCCs) prevented Ca^{2+} wave propagation.

Roose et al. (2006)
The system developed by Roose et al. (2006) to simulate Madin-Darby canine kidney cells was based on earlier models by (Wilkins and Sneyd reference)(Atri 1993 reference), and it accounts for a mechanism that allows Ca^{2+} to upregulate (increase) IP_3 production as well as downregulate it, unlike in Meyer and Stryer (1988),Meyer and Stryer (1991), which only accounts for positive feedback of Ca^2 on IP_3. Roose et al. (2006) established that for a single cell, low concentrations of Ca^{2+} can upregulate IP_3 formation, but Ca^{2+} at sufficiently high levels can downregulate IP_3 formation, in good agreement of experimental work of (Hirose et al.).

Shaikh et al. (2012)
The Shaikh et al. (2012) model is one of the most advanced calcium induced calcium release (CICR) models developed yet: it is a development of Koenigsberger et al. (2005). Since we are to benchmark our homogenised Goldbeter et al. (1990) model with Shaikh et al. (2012), it is worth exploring its mechanism and results in detail. Referring to figure (2.5) the cascade of molecular processes within an EC-SMC unit, numerically ordered, is:

1. Agonist binds to purinergic receptors (P_2Y) on EC membrane, activating G protein coupled receptor (GPCR), and hence activating membrane bound Phospholipase C (PLC) which catalyses hydrolysis of PIP_2 to IP_3, which is released into intracellular space.
2. IP_3 binds to IP_3R receptor located on SR membrane surface.
3. IP_3 bound IP_3R induces Ca^{2+} ion release from ER/SR into cytosol.
4. CICR: calcium induced calcium release. This released Ca^{2+} sensitises IP_3R further, causing yet more Ca^{2+} release into cytosol. Cytosol of EC and SMC is saturated with Ca^{2+} at this point, causing depolarisation of membrane potential.

5. SERCA pump (located on ER/SR membrane): replenishes ER/SR Ca^{2+} level. Low affinity binding sites located on cytosolic side of pump is activated by cytosolic Ca^{2+}, causing SERCA pump to pump Ca^{2+} back into ER/SR.

6. Ca^{2+} leakage from ER/SR is caused by Ca^{2+} concentration gradient difference between cytosol and ER/SR. Mechanism maintains Ca^{2+} equilibrium.

7. Non-selective ion channel in ECs allow influx of extracellular Ca^{2+}, due to cytosolic Ca^{2+}.

8. CaATPase pushes cytosolic $Ca2^{2+}$ out into extracellular space.

9. BK_{Ca}: large conductance Ca^{2+} activated K^+ channels allow efflux of K^+ from cytosol, activated by binding of cytosolic Ca^{2+}. Hyperpolarises membrane potential.

10. SK_{Ca}: small conductance Ca^{2+} activated K^+ channels allow efflux of K^+ from cytosol, activated by binding of cytosolic Ca^{2+}. Hyperpolarises membrane potential.

11. residual current contributes to membrane repolarisation.

12. IP_3 binds to IP_3R receptor of ER/SR in SMC. IP_3 is transmitted from EC to SMC through heterocellular coupling.

13. IP_3 induced together with CICR induced cytosol $Ca2^{2+}$ increase , depolarises SMC membrane potential, in much the same manner as for the EC.

14. VOCCs: voltage operated calcium channels in SMC opens upon depolarisation. VOCCs allow influx of $Ca2^{2+}$ into cytosol. But VOCCs close upon repolarisation of membrane potential.

15. NaCl exchanger expels $Ca2^{2+}$ from cytosol. Causes hyperpolarisation.

16. BK_{Ca}: large conductance Ca^{2+} activated K^+ channel opens upon Ca^{2+} binding. Efflux of K^+ causing repolarisation.

17. Cl^- influx contributes to repolarisation.

18. Homocellular communication can take place through Ca^{2+}, IP_3 and membrane potential.

19. heterocellular communication again, can take place through Ca^{2+}, IP_3 and membrane potential.

20. Hyperpolarisation in EC can spread to SMC, resulting in the closure of VOCCs in the SMC.

(Shaikh et al., 2012)

From this we can see that CICR together with SERCA uptake, is responsible for oscillations in time of cytosolic Ca^{2+} concentrations, or the 'intracellular

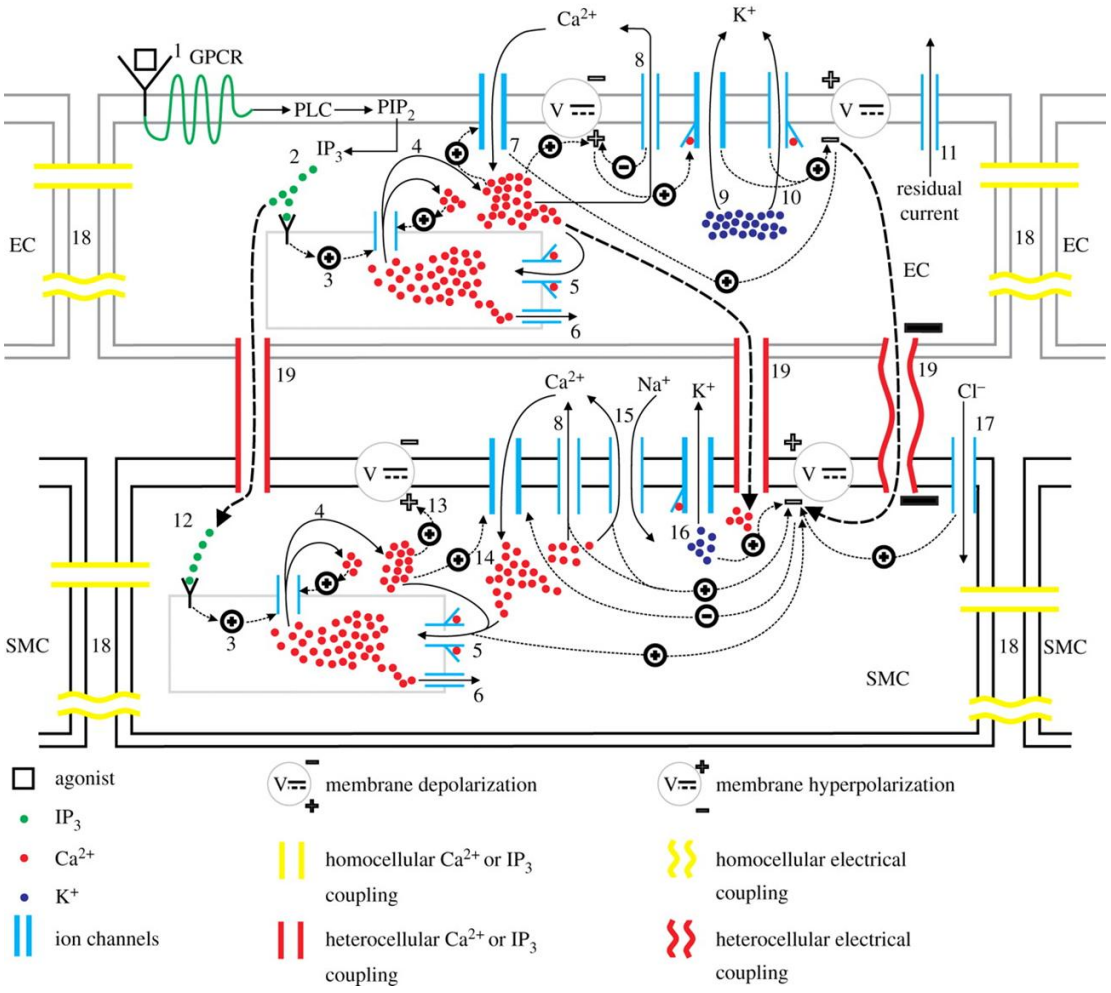

Figure 2.5: Diagram illustrates the cascade of biochemical processes following an agonist stimulation on the EC of a coupled EC-SMC unit, leading to hyperpolarisation/depolarisation of the cell. The role of various ion channels located on the membrane, and the different intercellular coupling channels are included.

oscillator'. BK_{Ca}, SK_{Ca}, Na/k, Na/Ca and VOCCs all act to generate the membrane oscillator: oscillations in the membrane potential of the cell.

The temporal Ca^{2+} oscillatory behaviour arising from the CICR mechanism of figure 2.5 may be analysed with a bifurcation diagram, (figure 2.6), showing how cytosolic Ca^{2+} for a single uncoupled SMC varies for the range of agonist stimulation $0.065 \leqslant J_{PLC_{agonist}} \leqslant 0.19$. Beginning from $J_{PLC_{agonist}} = 0.065$, the solution remains in stable steady state until $J_{PLC_{agonist}} = 0.075\mu M/s$, at which point a Hopf bifurcation occurs, where the solution undergoes a transition from stable steady state into stable limit cycle (oscillatory state). These temporal oscillations of Ca^{2+} concentration have constant oscillatory amplitude over time, and they continue until $J_{PLC_{agonist}} = 0.160\mu M/s$, where a second Hopf bifurcation takes place, and this time the bifurcation is that from an oscillatory state back to an steady state equilibrium state. So we have 3 domains separated by two Hopf bifurcations, that is, 1 oscillatory domain and two steady state domains.

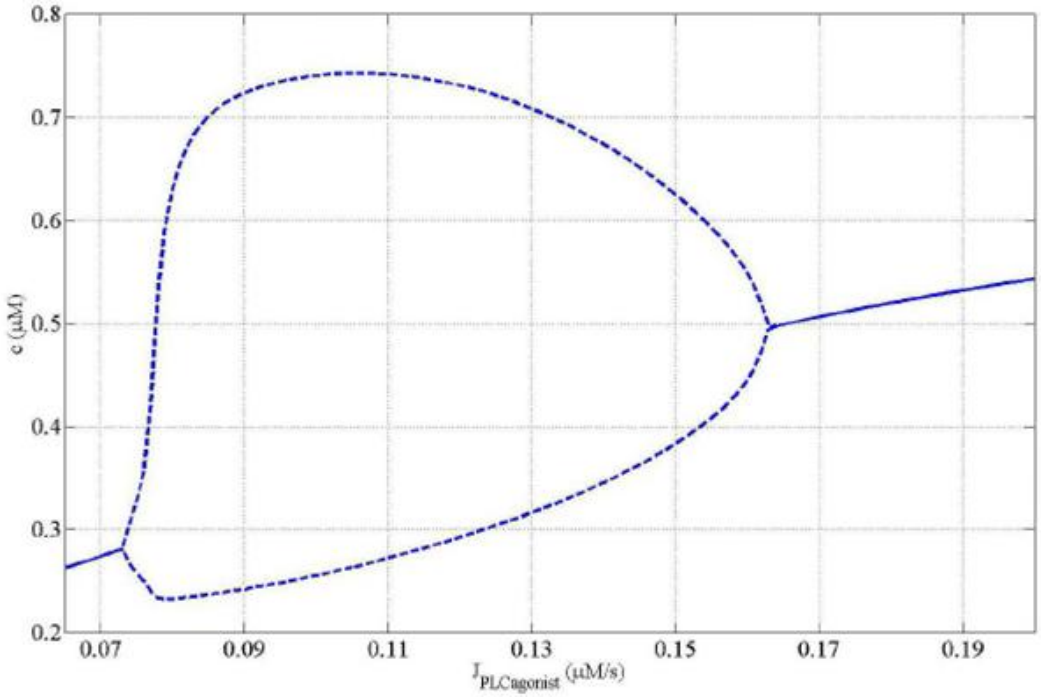

Figure 2.6: Bifurcation diagram, taken from Shaikh et al. (2012) shows effect of Ca^{2+} concentration (c) in a single uncoupled SMC to varying levels of $J_{PLC_{agonist}}$ stimulation in their model. A Hopf bifurcation occurs at $J_{PLC_{agonist}} = 0.075\mu M/s$, (bifurcation from steady state to oscillatory domain), and a second Hopf bifurcation is at $J_{PLC_{agonist}} = 0.160\mu M/s$ (bifurcation from oscillatory to non-oscillatory domain)

The major aim in the numerical experiments conducted by Shaikh et al.

(2012) was in understanding the Ca^{2+} dynamics in a 'physiologically relevant' arterial model. There are two major features of a simulated arterial model that make it a physiologically relevant one. Firstly its endothelial layer is stimulated with a spatially inhomogeneous agonist ATP concentration profile, specifically the profile is of a sigmoidal increase in ATP along the spatial domain, as shown in figure (2.7). This is a time-averaged profile which approximates the time dependent profile known to occur in atheroprone areas. Second, a sufficiently large population of coupled ECs and SMCs make up the arterial model, but how those ECs and SMCs are coupled determines the pathological state of the artery. Table (2.1) shows that depending on the IP_3, Ca^{2+}, and membrane potential coupling configurations of the cells, the arterial segment can be simulated to either be in a healthy state, in a pathological state of early arterosclerosis, or in a later stage of arterosclerosis. The reason behind this lies in connexin expression.

The expression of the 3 connexins $C \times 37$, $C \times 40$, $C \times 43$, vary according to the pathological state of the artery. (Refer to section reference). Further, the connexin composition of a gap junction determines its permeability to specific ions and molecules.

$C \times 37$ homotypic gap junctions, generally expressed in tissues of undisturbed flow, are highly selective in its preferential conductance of monovalent cations, although they have higher electric conductance than the respective $C \times 40$ and $C \times 37$ gap junctions. (Rackauskas et al., 2007b)

$C \times 40$ junctions also commonly found in tissues of undisturbed flow, tend to allow passage of divalent cations, Ca^{2+} for example.

$C \times 43$ being the least selective of the 3 connexins (and commonly observed in pathological arteries), even allows conductance of large molecules such as ATP and IP_3, but $C \times 43$ junctions have lower electrical conductance than the other 2 connexins. (Rackauskas et al., 2007b), (Goldberg et al., 2004), (Johnstone et al., 2009).

Recall that artherosclerosis is linked to disturbed flow regions, and that the cell calcium dynamics in such regions are found to be different to that of undisturbed regions. So an understanding of the Ca^{2+} dynamical behaviour of the artery in these atheroprone regions can give us an understanding of the biochemical role behind arterosclerosis.

Figure (2.8) shows the SMC $Ca2+$ concentrations along a healthy artery (case 1 in table 2.1) in a environment of disturbed flow (i.e. it is subjected to the sigmoid profile of figure (2.7)). In particular, figure (2.8) shows the temporal progression of these $Ca2+$ concentrations (at specific intervals in time). Initially, bands of Ca^{2+} waves can be seen around the region of linear ATP variation, surrounded by steady state Ca^{2+} levels on either side. As time progresses, these Ca^{2+} bands propagate into the region of artery subjected to a low and constant ATP stimulation. That is, the oscillatory waves travel to the upstream cells of the arterial segment, inducing oscillations in cells which were not originally in oscillation. As the waves propagate, they undergo 'band

case	SMC-SMC	EC-EC	SMC-EC	EC-SMC
1	V, Ca^{2+}, IP_3	V, Ca^{2+}	V, IP_3	V, IP_3
2	V, Ca^{2+}, IP_3	V, Ca^{2+}	V, Ca^{2+}, IP_3	V, Ca^{2+}, IP_3
3	V, Ca^{2+}, IP_3	V, Ca^{2+}, IP_3	V, Ca^{2+}, IP_3	V, Ca^{2+}, IP_3
4	V, Ca^{2+}, IP_3	IP_3	IP_3	IP_3

Table 2.1: Table shows that depending on the coupling configuration of ECs and SMCs, the arterial segment can be simulated to be in various pathological states. **case 1**: Simulates a healthy artery **case 2**: Simulates a healthy artery. Same configuration as case 1 except an additional heterocellular Ca^{2+} coupling enabled. **case 3**: Pathological state of early atherosclerotic lesion. Same configuration as case 2, except an additional homocellular EC IP_3 coupling introduced (to simulate $C \times 43$ expression). **case 4**: Pathological state of mature atherosclerotic lesion. Homocellular and heterocellular Ca^{2+} and membrane potential between ECs are abolished to simulate lack of $C \times 40$ and $C \times 37$.

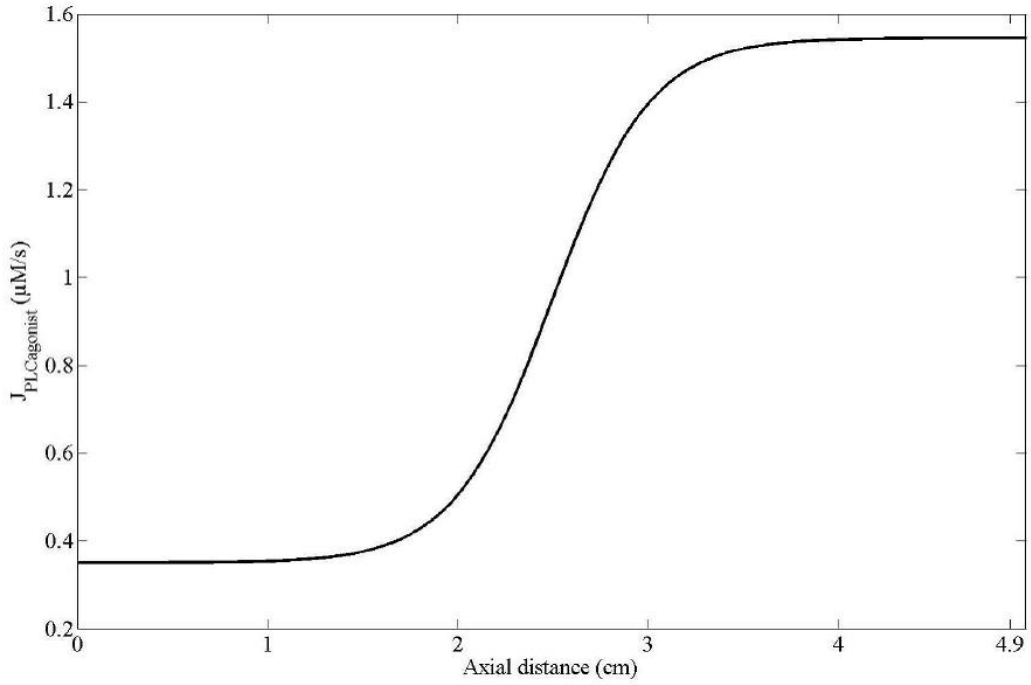

Figure 2.7: The spatial variation of agonist ATP $J_{PLC_{agonist}}$ to which the endothelial layer of the artery is subjected to, follows a sigmoid variation.

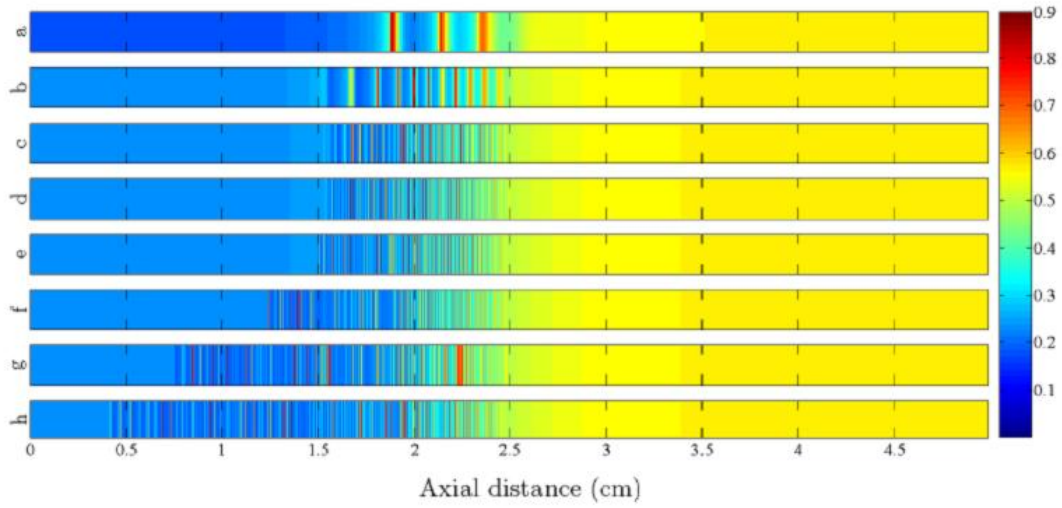

Figure 2.8: The time progression of SMC Ca^{2+} concentration along the artery, generated from the model of Shaikh et al. (2012). Vertical axis: time progression (at times 2.5, 4, 10, 20, 30, 60, 120 from (a) to (h)). Horizontal axis: length along artery. Colour bar indicates high concentrations (red) to low concentrations (blue). Note the wave band patterns of Ca^{2+} at time (a), that propagate to upstream parts of the arterial segment (b) to (h).

thinning', whereby the wavelength decreases. Band thinning is essential for the waves to propagate, and is caused by the concentration gradient of Ca^{2+} between neighboring cells. The gradient arises from neighbouring cells oscillating asynchronously with each other, so that there is transfer of Ca^{2+} between neighbouring SMCs as a result of this concentration gradient.

2.3.2 ICC IP_3-Ca^{2+} Cross Coupling Based Models

An important difference of the ICC mechanism to CICR, is that cytosolic IP_3 oscillations are required for Ca^{2+} oscillations in the cytosol. Another notable feature of ICC is the ability of cytolic Ca^{2+} to upregulate IP_3 (positive feedback step, as below). In the minimal model of Meyer and Stryer (1988), based on a single rat basophilic leukemia cell (RBL), there is a sequence of 4 steps forming the mechanism responsible for cytosolic calcium oscillations:

1. **Co-operativity**. Following hormone stimulation of the cell membrane receptor, and formation of IP_3, the binding of at least 3 molecules of IP_3 to ER channels causes a Ca^{2+} flux from the ER into the cytosol.

2. **Positive feedback**. The released cytosolic Ca^{2+} stimulates receptor activated phospholipase C (PLC), the enzyme that catalyses the hydrolysis of phosphatidylinositol 4,5-bisphosphate (PIP_2) into IP_3. This increase in IP_3 stimulates yet more Ca^{2+} to be released from ER. Besides the Ca^{2+} stimulated release of IP_3, the authors have also assumed the release of PLC through the hormone activation of a cell

surface G-protein receptor. The level of receptor activation was designated as the parameter R.

3. **Deactivation**. Mitochondrial sequestration of the cytosolic Ca^{2+} ions leads to a depletion of ER Ca^{2+} stores, as the IP_3 channels remain open. Cytosolic Ca^{2+} is lowered, leading to a decrease in IP_3 and ER channel closure.

4. **Reactivation**. The ER $Ca^{2+} - ATPase$ pump begins the uptake of cytosolic Ca^{2+} until a critical ER Ca^{2+} has been reached. Beyond this critical point, co-operativity and positive feedback begins another calcium peak. The time required for ER Ca^{2+} to reach the critical level determines the time interval between successive peaks.

The shape, amplitude and period between the calcium oscillations agreed well with experimentally determined results. Beyond a certain critical level of receptor activation (R), temporal oscillations in cytosolic Ca^{2+} become apparent, and the frequency of calcium peaks increases with increasing R, while the amplitude of these oscillations remain constant. Beyond $R = 44.5\%$ however, the excessively high levels of IP_3 (generated from the high PLC activation) maintains a constant opening of ER channels. This produces a steady state elevated Ca^{2+} level in the cytosol, and no oscillations are observed.

2.3.3 Biphasic Based Models

The single cell Xenopus laevis oocyte model developed by Atri et al. (1993), with cytosolic diffusion incorporated into it, is based on the biphasic response of ER bound IP_3 receptors (IP_3R) to cytosolic Ca^{2+}. That is, low and high levels of $[Ca^{2+}]_c$ can inhibit ER Ca^{2+} release, but intermediate $[Ca^{2+}]_c$ can allow for ER Ca^{2+} release. IP_3R has 3 binding domains: domain 1, domain 2 and domain 3, and it was assumed in their model that for activation of each of the domains, one IP_3 molecule is required to bind to domain 1, one Ca^{2+} has to bind to domain 2, while two Ca^{2+} is needed to bind to domain 3 for its activation. A Ca^{2+} flux from ER to cytosol will only occur if domains $1 and 2$ are activated and domain 3 is inactivated. The authors observed propagating circular $[Ca^{2+}]$ waves in a $250\mu m \times 250\mu m$ single cell when subjected to local IP_3 at the centre of the domain. Circular waves propagate outwards from the centre in a radial direction, while diminishing in magnitude as they do so. An important prediction from their work was that Ca^{2+} inactivation of IP_3R channels has to occur at least twice as slow as Ca^{2+} activation of IP_3R channels, otherwise propagating Ca^{2+} waves would not be observed. Atri et al. (1993) also generated spiral waves by introducing a refractory region ($[Ca^{2+}]$ is below its steady state value) to a region of a propagating circular wave.

Chapter 3

Homogenisation Theory and Methods

We wish to prove that homogenisation can be used as an alternative method of producing the same results as its corresponding discrete form. And we can only do so by developing a homogenised model and directly comparing its results with those from a discrete model which has already been implemented. Before doing so, we must understand how the homogenised form of a discrete model is derived mathematically. We shall understand this by using by way of example the discrete Shaikh et al. (2012) to formulate its corresponding homogenised PDE, which we refer to as a reaction diffusion equation. We will then go on to describe the various reaction diffusion equations that have been encountered in mathematical biology.

The remainder of the Chapter focuses on the numerical methodology we shall be using to implement the two models we are concerned with in this thesis: the Brusselator and the Goldbeter et al. (1990), which is a homogenised PDE.

3.1 Homogenisation Theory

In the macroscale model of Shaikh et al. (2012), 59904 SMCs and 23040 ECs were homocellularly and heterocellulary coupled to form the computational artery. And within each endothelial or smooth muscle cell were a set of ODEs to simulate the complex biochemical pathways occurring over time. These ODEs contain coupling terms to model the fluxes of chemical molecules between neighbouring cells. This is best illustrated by an example ODE: the rate of change of cytosolic Ca^{2+} within one smooth muscle cell:

$$\frac{dc}{dt} = J_{IP_3} - J_{SRUptake} + J_{CICR} - J_{EFF} + J_{LEAK} - \tag{3.1}$$

$$J_{VOCC} + J_{Na/Ca} + J_{Ca}^{SMC-SMC} + J_{Ca}^{SMC-EC} + J_{Ca}^{EC-SMC} \tag{3.2}$$

The reaction terms are:
J_{IP_3}: Flux of Ca^{2+} into cytosol

$J_{SRUptake}$: Uptake of cytosolic Ca^{2+} into SR.
J_{CICR}: Flux of Ca^{2+} into cytosol through CICR pathway.
J_{EFF}: Flux of Ca^{2+} out of cytosol through Ca-ATPase
J_{LEAK}: Flux of Ca^{2+} into cytosol through SR leakage
J_{VOCC}: Flux of Ca^{2+} into cytosol through VOCCs
$J_{Na/Ca}$: Flux of Ca^{2+} out of cytosol through Na/Ca exchanger

Refer to paper of Shaikh et al. (2012) for full mathematical formulae corresponding to these terms.
While the coupling terms are:
$J_{Ca}^{SMC-SMC}$: Homocellular SMC-SMC coupling.

J_{Ca}^{SMC-EC}: Heterocellular SMC-EC coupling.

J_{Ca}^{EC-SMC}: Heterocellular EC-SMC coupling.

Similar ODEs model the other state variables of the SMC, namely cytosolic IP_3, membrane potential, SR Ca^{2+}. When these ODEs are combined together, a more general form of representation would be:

$$\frac{d\underline{\Phi}_j}{dt} = R_j(\underline{\Phi}, t) + \sum_k C(\underline{\Phi}_j - \underline{\Phi}_k) \tag{3.3}$$

R and C denoting reaction and coupling terms respectively, and vector $\underline{\Phi}$ the vector containing all the various state variables. Subscript j indicates to which particular cell the ODEs belong to, while subscript k indicates which neighbouring cell it is coupling to.

In the process of homogenisation, if we denote n = total number of SMCs and ECs, and L =length of each cell, we seek to find:

$$lim_{n\to\infty, l\to 0} = n \times l = constant \tag{3.4}$$

such that the product $n \times l$ remains constant. In a homogenised model, there are two assumptions: firstly there is no intracellular diffusion of cell species, so only the intercellular diffusion of species through gap junctions exists and secondly, the concentrations of species within cells are spatially uniform, but the concentrations of species between cells are non-uniform. Incorporation of the reaction processes of equation 3.3 into 'Fick's' second law results in the reaction diffusion equation:

$$\frac{\partial\underline{\Phi}}{\partial t} = R(\underline{\Phi}, t) + \underline{D}\frac{\partial^2\underline{\Phi}}{\partial x^2} \tag{3.5}$$

Function R contains the reaction terms, vector $\underline{\Phi}$ again contains the different state variables and $\partial^2\underline{\Phi}/\partial x^2$ can be considered the replacement of the homocellular coupling term in equation (3.1), while $\underline{D}$ is the effective diffusion coefficient determining the strength of intercellular diffusion. Reaction Diffusion PDEs have a wealth of applications, especially in the field of mathematical biology as we shall see. The discretised form of equation 3.5 is:

$$\frac{d\underline{\Phi}}{dt} = R(\underline{\Phi}, t) + \frac{\underline{D}}{\delta x^2}\left(\underline{\Phi}_{i+1} + \underline{\Phi}_{i-1} - 2\underline{\Phi}_i\right) \tag{3.6}$$

From which we can equate the coupling coefficient of equation 3.3 with the diffusion term of equation 3.6: $\underline{D}/\delta x^2 = C$, where δx is the length of the discrete cell. From Shaikh et al. (2012) the length of a single EC is $\delta x = 100\mu m$, and gap junction permeability of Ca^{2+} and IP_3 were assumed to be $C = 0.05s^{-1}$ due to lack of experimental data, which gives $\underline{D} = 500\mu m^2 s^{-1}$.

It is important to clarify that the effective diffusion we use ($\underline{D}$), is different to that used by Keener and Sneyd (2009) and other authors. The effective diffusion they use (D_e) also account for the intracellular diffusion within cells:

$$\frac{1}{D_e} = \frac{1}{D} + \frac{1}{LF} \tag{3.7}$$

D: Diffusion coefficient of a single cell.
F: Gap junction permeability.
L: Distance between gap junctions.
(Keener and Sneyd, 2009)

Roose et al. (2006) incorporated this effective diffusion approach into their model of Kidney Epithelial cells, while Wilkins and Sneyd (1998) used the effective diffusion coefficient to model spiral waves.

In our homogenised models, the approach of equation (3.7) is not relevant, since our assumption of infinitely small cell lengths $l \to 0$ in equation (3.4) implies that cytosolic diffusion is not accounted for and thus we assume that it is an infinitely large value. The only diffusion taking place in our models is that of intercellular diffusion.

3.2 Reaction Diffusion Systems in Mathematical Biology

Reaction diffusion (RD) systems that model spatial temporal variation occur extensively in Biology. So many studies of these systems have taken place in recent years, and such a vast collection of literature has accumulated now, that the study of reaction diffusion equations in itself, has become a well-established subject in mathematical biology. As such the example reaction diffusion models we explore in this section are merely a sample of the vast context in with reaction diffusion mechanisms are applied in biology.

Consider below the general form for the reaction diffusion, where different systems arising from different biological context, have their own variations of this general form:

$$\frac{\partial \mathbf{u}}{\partial t} = f(\mathbf{u}) + D\nabla^2 \mathbf{u} \tag{3.8}$$

$\mathbf{u}$: Component or species of system.
$f(\mathbf{u})$: Reaction kinetics are typically non-linear, and contain parameters within the expression. Parameters which when varied, can cause bifurcations and have major effects on the behaviour of the system, as we shall see.

D: diffusion matrix containing the diffusion coefficients associated with each species.
$D\nabla^2\mathbf{u}$: diffusion term.

Consider the solutions of these RD mechanisms as falling into two broad categories: those classed as spatio-temporal varying patterns, that is travelling wave phenomena, and those classed as steady state but spatially non-uniform patterns. One such example of a steady state pattern can be seen in Morphogenesis. Turing suggested in 1952 in his well known paper, the concept of chemical morphogens reacting and diffusing through the tissue, as the mechanism behind the formation of the shape and form of a growing organism in Morphogenesis. (Turing, 1952).

$$u_t = D\frac{\partial^2 u}{\partial x^2} + ru\left(1 - \frac{u}{K}\right) \tag{3.9}$$

We begin our study of spatio-temporal patterns with the Fisher-Kolmogorov (KPP) equation equation 3.9, a one component, one dimension system that is one of the simplest cases of reaction diffusion. Even with such a basic model, there exists a travelling wave joining the two steady states u=0, u=1. Typical of multicomponent systems with multiple steady states are the existence of propagating waves that join the steady states together. Perhaps most interesting of all though, is the richness and variety of wave patterns that come out of multicomponent systems.

We only need to look at the 2 component Fitzhugh-Nagumo (FHN) model to see the existence of pulse waves that propagate out from the steady state before returning to it. The FHN, a simplified caricuture of the more detailed 4-variable Hodgkin-Huxley model (describing the excitable behaviour of axon cells), has been used in various physiological applications Murray J.D. (1989), namely atrial flutter and fibrillation (A.T., 1974), and reverberating cortical depression waves in the brain cortex. (M and J, 1974). In the Hodgkin-Huxley model, the cell lipid bilayer is represented by a capcitance, and voltage gated ion channels and ion pumps, together with sodium and potassium are involved in the generation of an action potential.

$$\frac{\partial u}{\partial t} = u(a-u)(u-1) - v + D\frac{\partial^2 u}{\partial x^2} \tag{3.10}$$

$$\frac{\partial v}{\partial t} = bu - \gamma v \tag{3.11}$$

u: referred to as the fast variable, it is related to the membrane potential
v: referred to as the slow variable. It is associated with terms involving sodium, potassium and other ions that contribute to the membrane potential.
D: Diffusion coefficient associated with the axial current in the axon.

Note that the FHN demonstrates excitable behaviour. Excitable in that these pulse waves only appear if we exceed a certain threshold perturbation in component u.

One of the more well known reactions is the Belousov-Zhabatinskii (BZ) reaction in which we can witness what is known as a 'target pattern', a circular wave radiating from a high bromous acid concentration to a low bromous acid concentration. Again, a two component system:

$$\frac{\partial x}{\partial t} = k_1 ay - k_2 xy + k_3 a_x - k_4 x^2 + D\frac{\partial^2 x}{\partial s^2} \tag{3.12}$$

$$\frac{\partial y}{\partial t} = -k_1 ay - k_2 xy + D\frac{\partial^2 y}{\partial s^2} \tag{3.13}$$

x: Concentration of bromous acid.
y: Concentration of bromide ion.
k: Rate constants.

A different wave pattern also seen to occur in the BZ is the 'spiral wave', whereby a wave is seen to propagate from its current position on a circle as it rotates around the circle, thus giving a spiral appearance. Müller et al. (1985) demonstrates how these spiral patterns can clearly be visible on a thin layer of a BZ reagent placed within a petri dish. Importantly, spiral waves occur in the fields of cardiology and neurobiology, and also in the slime mould Dictyostelium. (P.C., 1983). Agladze and Krinsky (1982) however, presents higher order symmetry rotating structures than those of the BZ spirals: namely multi-armed vortices seen in a chemical medium placed in a petri-dish.

Maini (1995) gives an diverse collection of the practical problems that involve wave phenomena. In one of these studies, it is emphasized how travelling waves can give us an understanding of the biology of wound healing, specifically surface would healing in the cornea. Quite simply, wave fronts of cells and EGF: epidermal growth factor (regulates the cell migration and proliferation so critical to wound healing), move with constant speed and shape from an unwounded region to a wounded region of the cornea.

3.3 Numerical Methodology

Our goal is to implement a homogenised PDE model from the discrete Goldbeter et al. (1990). The PDE itself is a reaction diffusion system. Before we do that, we will complete a full analytical and numerical analysis of the 'Brusselator', with the intention that it will provide us with a better understanding of reaction diffusion systems in general. The PDE form of the Brusselator (derived from its ODE form) exhibits oscillatory solutions, and because of the diffusion term incorporated into it, spatio-temporal oscillatory patterns may be seen. This property is normally observed in the reaction diffusion systems of interest to us, and thus make the Brusselator a suitable preliminary study. In particular, we hope to understand how the system parameters influence the oscillatory solutions, and how diffusion affects spatio-temporal patterns, these findings we hope will offer us an intuitive feel for the way solutions of Goldbeter et al. (1990) behave. Further, the system only has two variables and 2 system parameters, making it a very simple

minimal model to implement. Note that the Brusselator is merely a theoretical set of equations: it has no physiological relevance to real cells, and is dimensionless.

3.3.1 Brusselator Numerical Methodology

The system below is that of the Brusselator ODE, and it has oscillatory solutions for parameter values of $B > 1 + A^2$. This ODE is

$$\frac{d\phi}{dt} = A + \phi^2\psi - B\phi - \phi \tag{3.14}$$

$$\frac{d\psi}{dt} = B\phi - \phi^2\psi \tag{3.15}$$

ϕ: dimensionless variable
ψ: dimensionless variable
A: parameter
B: parameter. Oscillatory solutions occur for $B > 1 + A^2$

An additional spatial dimension is incorporated into equations (3.14),(3.15), essentially transforming the original ODE system into that of a PDE. To avoid confusion we refer to them separately as the *brusselator ODE* and the *brusselator reaction diffusion PDE*.

$$\frac{\partial\phi}{\partial t} = D_1\frac{\partial^2\phi}{\partial^2 x} + A + \phi^2\psi - \phi(B+1) \tag{3.16}$$

$$\frac{\partial\psi}{\partial t} = D_2\frac{\partial^2\psi}{\partial^2 x} + B\phi - \phi^2\psi \tag{3.17}$$

With the spatial dependency, we have 2 additional parameters D_1 and D_2 which are the diffusion coefficients accounting for the strength of diffusion across the spatial domain.

Brusselator ODE There is no spatial dependency, the parameter A we set to be A=1 without loss of generality, and oscillatory solutions occur for $B > 1 + A^2$. So with our value of A, we expect a bifurcation to occur at B=2, beyond this critical point, a limit cycle should appear in the phase portrait of ϕ and ψ, resulting from the oscillatory solutions. We implement the equations in C program using the Trapezoidal Rule to provide time stepping. The major advantage in this approach being that trapezoidal time stepping is very similar to the Crank-Nicholson time stepping we will use for the brusselator reaction diffusion (RD) PDE. So solving the Brusselator ODE with this approach should provide us with ample insight into how best to implement the slightly more complex Reaction Diffusion PDE. (Pal, 2009) offers a comprehensive reference to the Trapezoidal Rule.

Standard application of the Trapezoidal Rule to (3.14) and (3.15):

$$\phi^{n+1} - \frac{h}{2}\left[(\phi^{n+1})^2\psi^{n+1} + B\phi^{n+1} + \phi^{n+1}\right] = \phi^n + \frac{h}{2}\left[(\phi^n)^2\psi^n - B\phi^n - \phi^n\right] + h \tag{3.18}$$

$$\psi^{n+1} - \frac{h}{2}\left[B\phi^{n+1} - (\phi^{n+1})^2\psi^{n+1}\right] = \psi^n + \frac{h}{2}\left[B\phi^n - (\phi^n)^2\psi^n\right] \tag{3.19}$$

h: The time step in the Trapezoidal time stepping.
Superscript n: denotes a discrete time point. n+1 is the current time, while n is the previous time.

In the computational implementation, we incorporate variables ϕ and ψ into a single one-dimensional array, $\underline{\Omega}$, such that $\underline{\Omega} = (\Omega_1, \Omega_2) = (\phi, \psi)$. This eliminates the complication arising from the $\phi^2\psi$ term in the system. We use Newtons method to seek the solutions:

$$J_f(\underline{\Omega}) \times \delta(\underline{\Omega}) = -\underline{F}(\underline{\Omega}) \tag{3.20}$$

$J_f(\underline{\Omega})$: The Jacobian matrix (arising from Newtons method) of the system, (equations (3.18), (3.19)), evaluated for a particular $\underline{\Omega}$.
$\underline{F}(\underline{\Omega})$: the system, (equations (3.18), (3.19)), evaluated for a particular $\underline{\Omega}$.
$\delta(\underline{\Omega})$: the error vector. The difference of $\underline{\Omega}$ before and after one Newton iteration. Added to the original $\underline{\Omega}$ (before the iteration) to update to a more accurate solution $\underline{\Omega}$.

A matrix approach is used to solve equation (3.20), where the Jacobian components $J_f(\underline{\Omega})$, along with the values of $-\underline{F}(\underline{\Omega})$ are placed together into an augmented matrix, with $-\underline{F}(\underline{\Omega})$ being the last column. A series of Gaussian eliminations of the augmented matrix yields $\delta(\underline{\Omega})$. $\delta(\underline{\Omega})$ is then added to $\underline{\Omega}$ to update it. This completes one Newton iteration. The matrix is setup again, with the new updated $\underline{\Omega}$, and a new iteration begins. Sufficient Newton iterations provide sufficiently converged solutions for $\underline{\Omega}$, in between each time step.

Brusselator PDE
Crank-Nicholson method is used to discretise the Brusselator PDE.

$$\frac{\partial\phi}{\partial t} = D_1\frac{\partial^2\phi}{\partial^2 x} + A + \phi^2\psi - \phi(B+1) \tag{3.21}$$

$$\frac{\partial\psi}{\partial t} = D_2\frac{\partial^2\psi}{\partial^2 x} + B\phi - \phi^2\psi \tag{3.22}$$

D_1 : Non unitary diffusion coefficient associated with variable ϕ
D_2 : Non unitary diffusion coefficient associated with variable ψ
B: spatially non-uniform parameter. Discussed in the following section
A: As with the Brusselator ODE, we set A=1 without loss of generality.

After the appropriate Crank-Nicholson discretisation of the system:

$$\begin{aligned}\phi_i^{n+1} - D_1\frac{\delta t}{2\delta x^2}[\phi_{i-1}^{n+1} - 2\phi_i^{n+1} + \phi_{i+1}^{n+1}] - \frac{\delta t}{2}[A + \left(\phi_i^{n+1}\right)^2(\psi_i)^{n+1} - \phi_i^{n+1}(1+B_i)] \\ = \phi_i^n + D_1\frac{\delta t}{2\delta x^2}[\phi_{i-1}^n - 2\phi_i^n + \phi_{i+1}^n] + \frac{\delta t}{2}[A + (\phi_i^n)^2(\psi_i)^n - \phi_i^n(1+B_i)]\end{aligned}$$

$$\psi_i^{n+1} - D_2\frac{\delta t}{2\delta x^2}[\psi_{i-1}^{n+1} - 2\psi_i^{n+1} + \psi_{i+1}^{n+1}] - \frac{\delta t}{2}B_i\phi_i^{n+1} + \frac{\delta t}{2}\left(\phi_i^{n+1}\right)^2(\psi_i)^{n+1} =$$
$$\psi_i^n + D_2\frac{\delta t}{2\delta x^2}[\psi_{i-1}^n - 2\psi_i^n + \psi_{i+1}^n] + \frac{\delta t B_i\phi_i^n}{2} - \frac{\delta t}{2}\left(\phi_i^n\right)^2(\psi_i)^n$$

δt: time step interval
δx: spatial step interval.
Superscript n: current time point.
Superscript n+1: forward time point.
Subscript i: spatial point, where $i = 1..N$, such that N is the total number of discrete spatial points.

We use 'no-flux' boundary conditions, where $\partial/\partial x = 0$ at the boundaries, and in the case of ϕ_{i-1} for $i = 1$, we set $\phi_0 = \phi_1$. This is referred to as a 'ghost point'. Likewise in the case of ϕ_{i+1} for $i = N$, we set $\phi_{N+1} = \phi_N$

In the computational implementation, we incorporate variables ϕ and ψ into a single one-dimensional array, $\underline{\Omega}$, such that:

$$\begin{aligned}\underline{\Omega}^{N+1} &= (\Omega_1, \ldots \Omega_i, \ldots \Omega_N, \Omega_{N+1}, \ldots \Omega_{N+i}, \ldots \Omega_{2N}) \\ &= (\phi_1, \ldots \phi_i, \ldots \phi_N, \psi_1, \ldots \psi_i, \ldots \psi_N)\end{aligned}$$

This eliminates the complication arising from the $\phi^2\psi$ term in the system. We use Newtons method to seek the solutions:

$$J_f(\underline{\Omega}) \times \delta(\underline{\Omega}) = -\underline{F}(\underline{\Omega}) \tag{3.23}$$

The iterative methodology remains the same as for the brusselator ODE.

3.3.2 Goldbeter Numerical Methodology

The Goldbeter system (Goldbeter et al. (1990)) is the simplest CICR system that has been developed, as it incorporates only the sufficient components to generate calcium oscillations. We shall first describe the biochemical pathway behind these oscillatory solutions, before presenting the set of equations describing the system. Then, we will explain how the system is discretised using the well established 'method of lines', and implemented in Matlab software environment.

Following agonist stimulation, the chemical cascade responsible for Ca^{2+} oscillations is (refer to figure 3.1 for a graphical representation):

1. Agonist attaches to a cell surface receptor (R), and activates a G protein (Gp). Phospholipase C (PLC) also activates. PLC catalyses the the hydrolysis of PIP_2 to IP_3 and diacylglycerol (DG). IP_3 is released into cytosol at this point.

2. Cytosolic IP_3 attaches to receptors on IP_3 sensitive pool, and Ca^{2+} is released into the cytosol from this pool.

3. Cytosolic Ca^{2+} activates ryodine receptors on the Ca^{2+}-sensitive pool to release yet more Ca^{2+} into the cytosol. A large peak in cytosolic Ca^{2+} can thus be observed.

4. Following the peak in cytosolic Ca^{2+}, $Ca^{2+} - ATPase$ pump on the Ca^{2+} sensitive store begins the re-uptake of cytosolic Ca^{2+} back into the store. Extracellular influx of Ca^{2+} into cytosol also contributes to this replenishment. A passive Ca^{2+} leak from this store into the cytosol is also accounted for in the model.

5. All the while there is a constant influx of extracellular Ca^{2+} into cytosol (removal of which eventually suppresses Ca^{2+} oscillations), and a linear efflux of Ca^{2+} from cytosol to extracellular space.

So we can see that cytosolic calcium (Ca^{2+}) oscillations arise from the cycling of calcium into and out of the calcium sensitive store. Further, cytosolic Ca^{2+} can spread to neighbouring cells (which are in a non-oscillatory state) through gap junctions to induce oscillations in these cells. As illustrated above, this is achieved through activation of receptors by Ca^{2+} in Ca^{2+}-sensitive pool.

$$\frac{\partial Z}{\partial t} = D1\frac{\partial^2 Z}{\partial x^2} + v_0 + v_1\beta - \underbrace{V_{M2}\frac{Z^n}{K_2^n + Z^n}}_{v_2} + \underbrace{V_{M3}\frac{Y^m}{K_R^m + Y^m}\frac{Z^p}{K_A^p + Z^p}}_{v_3} + k_f Y - kZ \tag{3.24}$$

$$\frac{\partial Y}{\partial t} = \underbrace{V_{M2}\frac{Z^n}{K_2^n + Z^n}}_{v_2} - \underbrace{V_{M3}\frac{Y^m}{K_R^m + Y^m}\frac{Z^p}{K_A^p + Z^p}}_{v_3} - k_f Y \tag{3.25}$$

Z: Cytosolic free Ca^{2+} concentration.
Y: Ca^{2+} concentration in the Ca^{2+}-sensitive pool.

v_0 and kZ: respectively are influx of Ca^{2+} into the cell, and efflux of Ca^{2+} out of cell. These fluxes are independent of external stimulation. v_0 is assumed constant while kZ is a linear variation.

v_2: The rate of $Ca^{2+} - ATPase$ pumping of Ca^{2+} from cytosol into Ca^{2+}-sensitive store. This process is in the form of a Hill equation with V_{M2} the maximum rate of pumping. The co-operativity coefficient is denoted by n. K_2 is the threshold constant for pumping.

v_3: The rate of release of Ca^{2+} from Ca^{2+} sensitive store into cytosol, described by the product of 2 Hill equations. V_{M3} denotes the maximum rate of Ca^{2+} release from this store. K_R and K_A are threshold constants for release and activation, respectively. The degree of activation cooperativity is p, while m is the cooperativity coefficient.

$v_1\beta$: The magnitude of Ca^{2+} release from IP_3 sensitive pool, where β is the saturation parameter for the IP_3 receptor, denoting the level of receptor

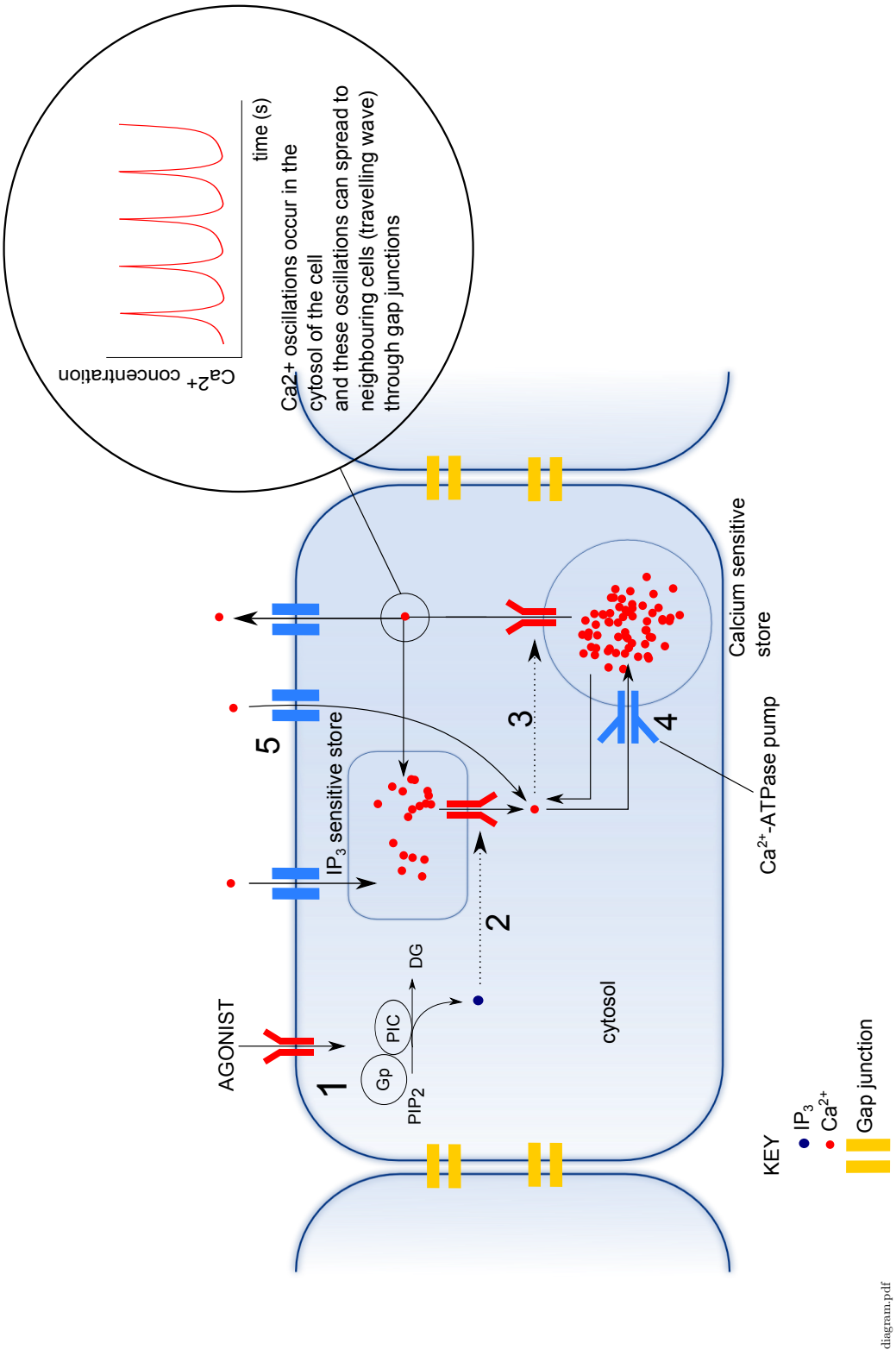

Figure 3.1: Diagram shows the cascade of biochemical steps responsible for generating calcium oscillations. This is the minimal CICR based model of Goldbeter et al. (1990), and we will be developing the homogenised form of this in our work. Diagram created using Inkscape. Jimmy Shek. Homogenised Models of SMCs and ECs. 2013

activation by IP_3.

These are the values set for the parameters, and they are within a physiological range:
$v_0 = 1\mu Ms^{-1}; v_1 = 7.3\mu Ms^{-1}; k = 10s^{-1}; k_f = 1s^{-1}; K_A = 0.9\mu M; K_R = 2\mu M; K_2 = 1\mu M; m = 2; n = 2; p = 4; V_{M2} = 65\mu Ms^{-1}; V_{M3} = 500\mu Ms^{-1};$

We may write equations 3.24 and 3.25 in the more general form as:

$$\frac{\partial Z}{\partial t} = D1\frac{\partial^2 Z}{\partial x^2} + f(Z, Y) \tag{3.26}$$

$$\frac{\partial Y}{\partial t} = g(Z, Y) \tag{3.27}$$

In the 'method of lines', only the right hand side of the equation is discretised, so that the PDE is reduced to a system of ODEs (equations 3.28 and 3.29). We can then proceed to use Matlab's ODE15s function to solve the system of ODEs.

$$\frac{dZ}{dt} = \frac{D1}{\delta x^2}[Z_{i+1} + Z_{i-1} - 2Z_i] + f(Z_i, Y_i) \tag{3.28}$$

$$\frac{dY}{dt} = g(Z_i, Y_i) \tag{3.29}$$

Where $1 \leq i \leq N$

Subscript i: spatial point, where i=1..N, such that N is the number of discrete spatial points.
δx: spatial step interval.

We use 'no-flux' boundary conditions, where $\partial/\partial x = 0$ at the boundaries, and in the case of Z_{i-1} for $i = 1$, we set $Z_0 = Z_1$. This is referred to as a 'ghost point'. Likewise in the case of Z_{i+1} for $i = N$, we set $Z_{N+1} = Z_N$

The data structure was arranged in a similar way as for the Brusselator PDE, where variables Z and Y were incorporated into a single one-dimensional array, $\underline{C}$:

$$\begin{aligned}\underline{C}^{N+1} &= (C_1, \ldots C_i, \ldots C_N, C_{N+1}, \ldots C_{N+i}, \ldots C_{2N}) \\ &= (Z_1, \ldots Z_i, \ldots Z_N, Y_1, \ldots Y_i, \ldots Y_N)\end{aligned}$$

As shown the diffusion term of equation (3.24) is discretised using a second order central difference scheme. This discrete diffusion term is entered into Matlab in the form of a matrix, M multiplied by a vector V. That is:

$$M \cdot V = [Z_{i+1} + Z_{i-1} - 2Z_i] \tag{3.30}$$

where if we take for the sake of example $i = 1..6$.

$$\begin{pmatrix} -1 & 1 & 0 & 0 & 0 & 0 \\ 1 & -2 & 1 & 0 & 0 & 0 \\ 0 & 1 & -2 & 1 & 0 & 0 \\ 0 & 0 & 1 & -2 & 1 & 0 \\ 0 & 0 & 0 & 1 & -2 & 1 \\ 0 & 0 & 0 & 0 & 1 & -1 \end{pmatrix} \begin{pmatrix} Z_1 \\ Z_2 \\ Z_3 \\ Z_4 \\ Z_5 \\ Z_6 \end{pmatrix} = [Z_{i+1} + Z_{i-1} - 2Z_i] \quad (3.31)$$

We may utilise Matlab's built in optimisation functions to exploit the sparsity of matrix M, so that computational time may be significantly reduced.

Chapter 4

Results and Discussion

4.1 Oscillations are Present in Brusselator ODE

The Brusselator ODE was simulated with parameter A set to $A = 1$ without loss of generality, and we established that oscillatory solutions occur for $B \geq 2$, while for $B < 2$ the system exhibits steady state solutions. The oscillatory solutions when $B = 3$ are shown in figure 4.1. Generally for oscillatory solutions, we found that an increase in parameter B results in an increase in wavelength, a decrease in frequency, and an increase in amplitude.

4.2 Spatio-temporal Patterns in Brusselator PDE

For the Brusselator Reaction Diffusion PDE, we investigated the effects of non-unitary diffusion ($D_1 \neq D_2 and D_1, D_2 \neq 0$) on the oscillatory behaviour of the system. The parameter B was assumed spatially inhomogeneous while A was set A=1 without loss of generality. 3 different configurations for non-unitary diffusion were considered:

- case 1: diffusion is abolished completely, $D_1 = 0, D_2 = 0$
- case 2: D_1 is increased while $D_2 = 0$
- case 3: D_2 is increased while $D_1 = 0$

In case 1 of no diffusion $D_1 = 0, D_2 = 0$, solutions generate the spatio-temporal pattern in figure (4.4). For a particular point along the spatial domain, there are oscillatory waves of ϕ as time progresses. As such, along the entire spatial domain, there are a series of asynchronous temporal oscillations: they are asynchronous both in frequency and in amplitude. This spatio-temporal patterning is consistent with the relation between parameter B with frequency and amplitude, as established from the results of the brusselator ODE. Recall that with increasing B, the amplitude of oscillations increases, while their frequency decreases. Indeed, in (figure 4.4), when subjected to the B parameter profile of (figure 4.2), the maximum amplitude oscillations occur at 10 units along the spatial domain (where B is maximal),

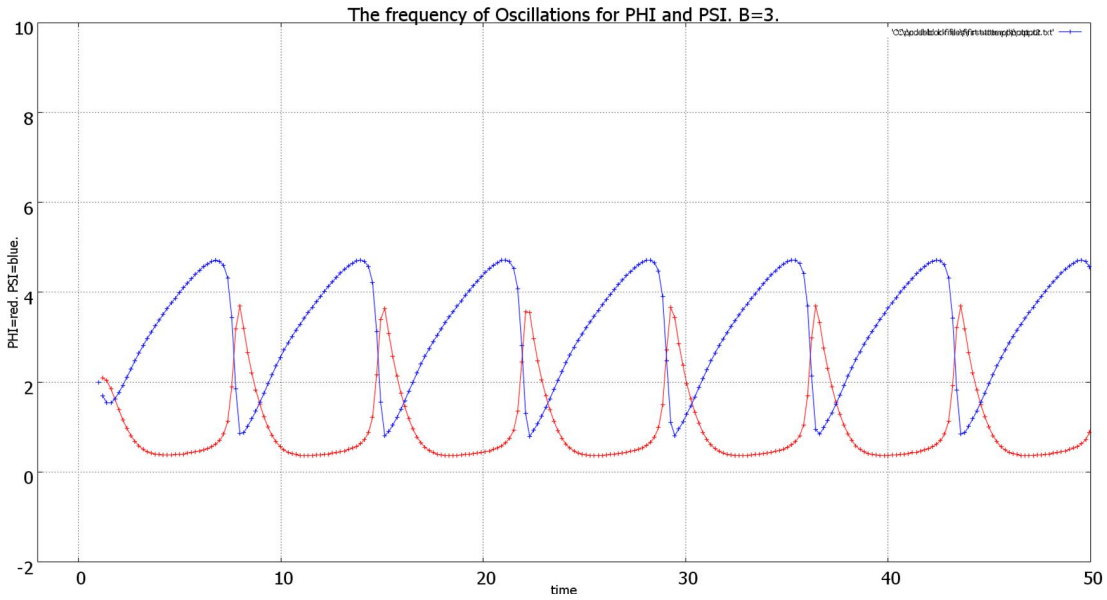

Figure 4.1: Time solutions of ϕ (red) and ψ (blue) for $B = 3$ $A = 1$. Note the bifurcation point for oscillatory behaviour lies at $B = 1 + A^2$. The frequencies of the oscillatory solutions of ϕ and ψ both oscillate completely out of phase. Generally for Brusselator oscillatory solutions, an increase in parameter B results in an increase in wavelength, a decrease in frequency, but an increase in amplitude.

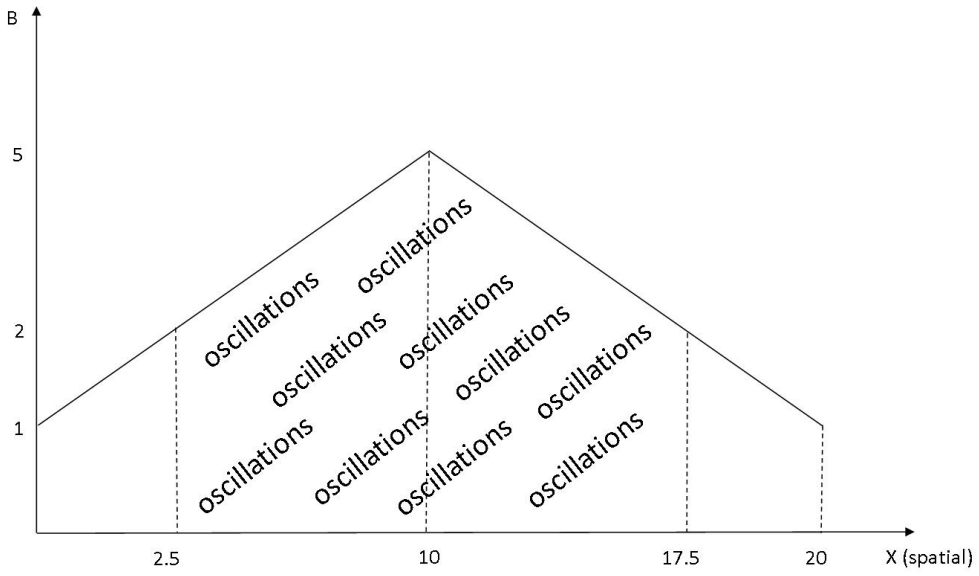

Figure 4.2: A linear variation of parameter B along the spatial domain. For $x < 10$, $B(x) = 0.4x + 1$, while for $x \geq 10$ $B(x) = -0.4x + 9$ For our system, oscillatory solutions are present for $B > 2$ (given that A=1).

and either side of this maximum, oscillations decrease linearly in amplitude, until there are no oscillations present at 0 units and 20 units spatially. Further, for a given time interval the wavenumber at spatial=10 for example is less than the wavenumber at spatial=4, reflecting the decrease in frequency with increasing B. Visually, the presence of the asynchrony in frequency gives rise to the 'V'-shaped lines seen in figure (4.4). On the contrary, if the oscillatory waves were to oscillate with uniform frequency along the spatial domain, then in theory straight lines parrallel to the spatial axis of the graph would be observed.

For case 2 ($D_1 = 0.05$ and $D_2 = 0$), figure (4.7) suggests that an increase in D_1 can synchronise the oscillations along space. Relative to figure (4.4), we can see in figure (4.7) how any two neighbouring points along space have time oscillations that are *relatively* more synchronised than those of figure (4.4). This is reflected in the nature of the lines seen in figure (4.7), notice how they are almost parallel to the spatial axis of the graph compared to the lines of figure (4.4). Simulation of figure (4.7) was re-run for longer duration of time= $400s$, and the same pattern is sustained, suggesting they are stable oscillations.

Results for case 3 (D_2 increase, $D_1 = 0$) suggest that in fact D_2 abolishes time oscillations. Figure (4.6) (where D_2 is increased to $D_2 = 0.02$) shows the break down of the temporal oscillatory waves. Larger values of D_2 cause oscillations to break down quicker.

Other Experiments
A physiologically relevant sigmoidal profile (similar to that used in Shaikh et al. (2012) was also implemented. That is, parameter B varies sigmoidally as opposed to linearly along the spatial domain. As with the linear profile the same 3 cases of diffusion configurations were again implemented, and the system produced the same behaviour.

A spatially varying piecewise function for parameter B (shown in figure 4.3) was applied to the Brusselator PDE system for a range of diffusion coefficients $\sim O(0.1)$. That is, $D1$ ranged from 0.1 - 2.0 in intervals of 0.1. The purpose of this was to test for the existence of travelling waves. No evidence for such waves were found.

Summary We have investigated in this section, the effects the diffusion coefficients ($D_1 and D_2$) have on the qualitative behaviour of the Brusselator PDE system. We have found that D_1 has the effect of synchronising oscillating solutions along a $1-$dimensional simulation domain, while D_2 in fact abolishes oscillating solutions so that a steady state and spatially heterogeneous solution persists. We have also attempted to prove the existence of travelling wave train solutions, although without success. We believe the reason for this was that the values of the diffusion coefficients and parameters A and B were not varied over a wide enough range. It may well be possible that a particular range of values for the parameters may generate wave train solutions in the system. Further investigation is required in order to elucidate this.

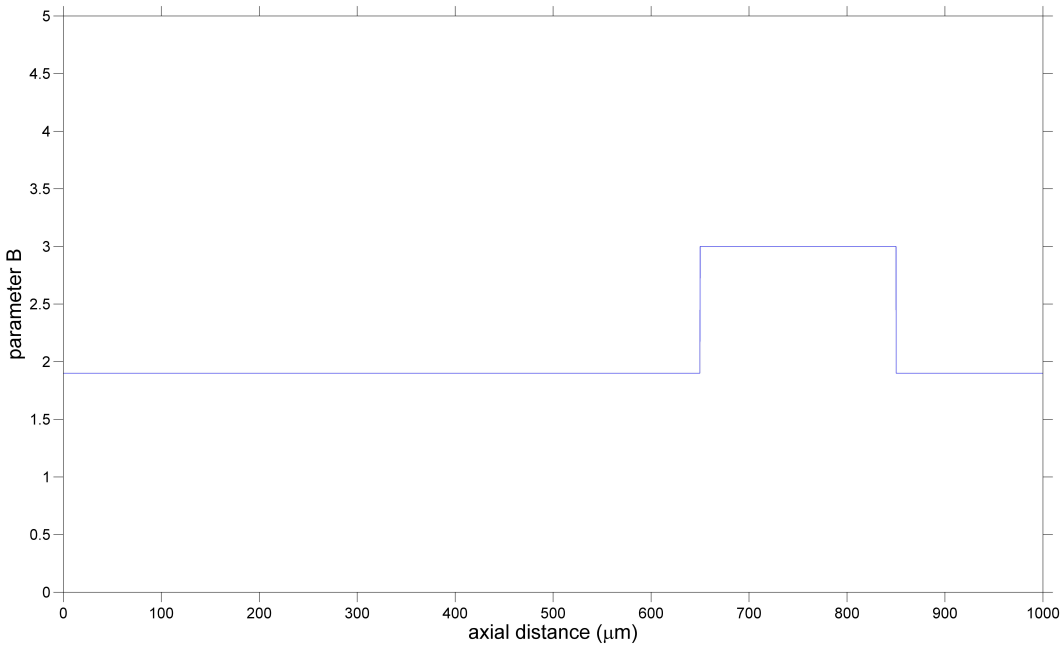

Figure 4.3: Piecewise spatial variation of paramter B. The elevated region corresponds to B= 3, the value for which oscillatory solutions occur, while for the rest of the domain, B= 1.9 corresponds to steady state solutions. This profile was applied to the Brusselator PDE system for a range of different diffusion coefficients, in order to find numerical evidence for propagating waves.

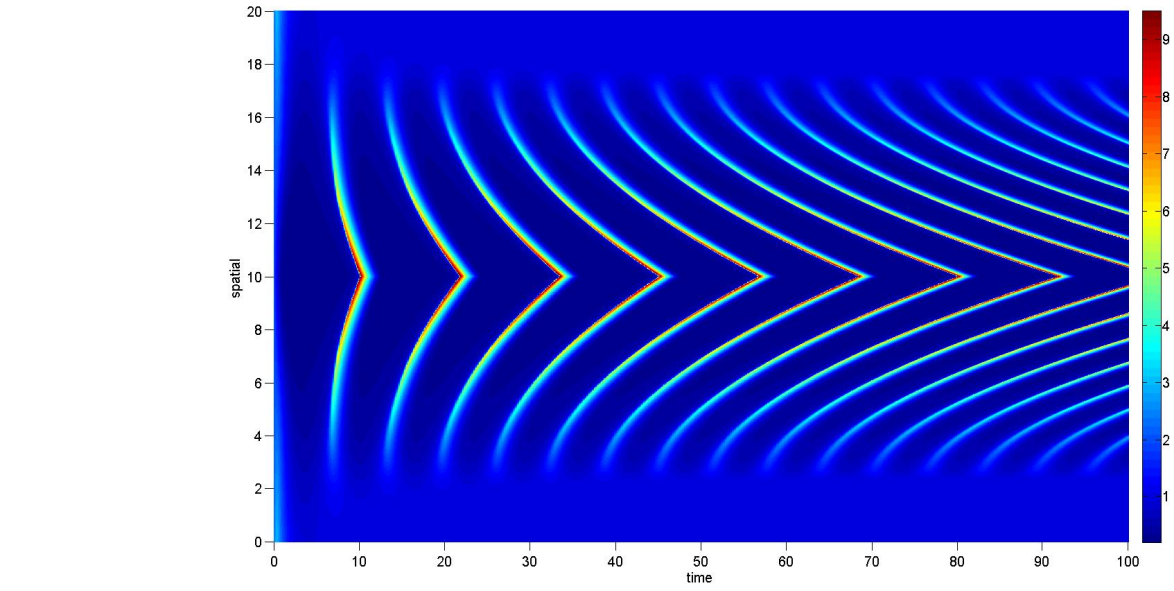

TERM BRUSSELATOR/NODIFF.jpg

Figure 4.4: Plot shows ϕ solutions across space-time domain. System is subject to a piecewise linear spatial variation in parameter B (figure 4.2). $D_1 = 0$ and $D_2 = 0$. Temporal oscillations at different points along spatial domain are out of phase with each other.

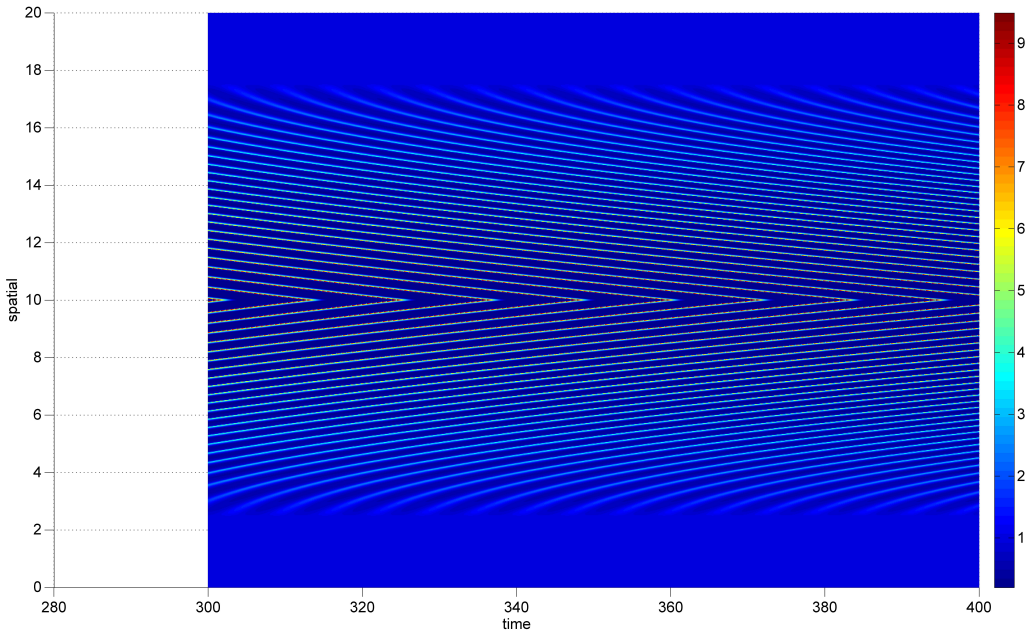

Figure 4.5: Same simulation as figure 4.4 but for longer duration of time= 400. Only last 100 time shown. It appears that the spatio-temporal pattern in figure 4.4 is only a temporary transient, where eventually the system settles down to the pattern shown in this figure.

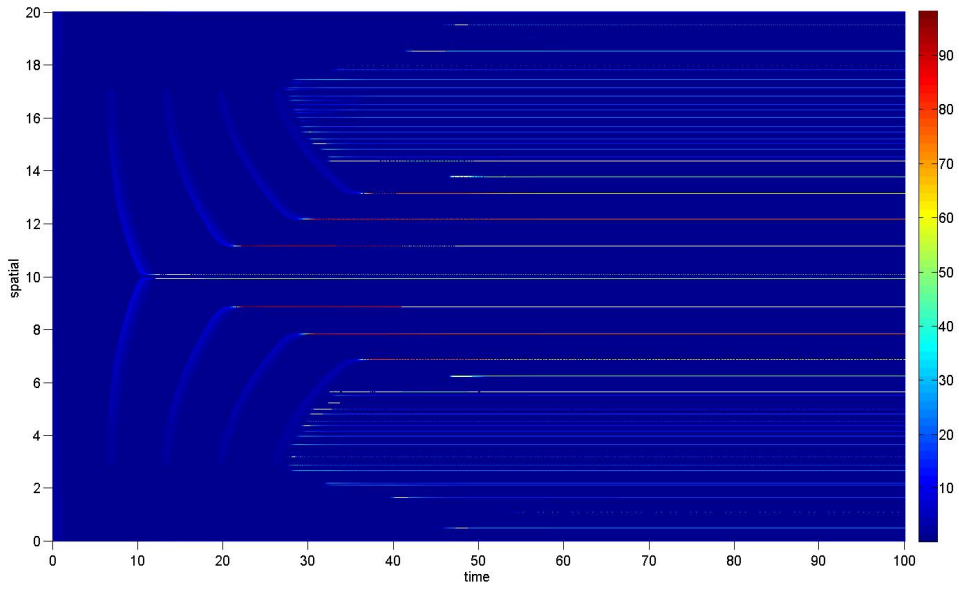

Figure 4.6: Plot shows ϕ solutions across space-time domain. System is subject to a linear spatial variation in parameter B (figure 4.2). $D_1 = 0$ and $D_2 = 0.02$. The temporal oscillations break down as spatially heterogenous steady state patterns form. Simulation was run for a longer time (time=400s), and these spatial patterns remain, suggesting they are persistent patterns.

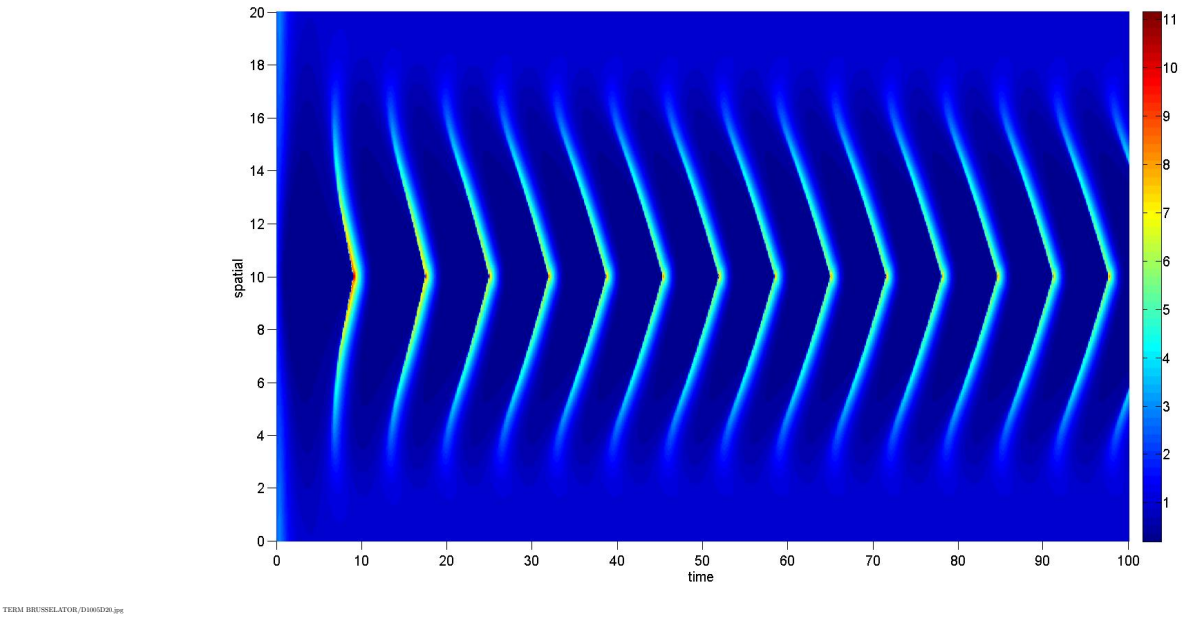

TERM BRUSSELATOR/D100SD20.jpg

Figure 4.7: Plot shows ϕ solutions across space-time domain. System is subject to a linear spatial variation in parameter B (figure 4.2). $D_1 = 0.05$ and $D_2 = 0$. Temporal oscillations at different points along spatial domain are more synchronised with each other, compared to those of [figure 4.4]. These oscillatory patterns persist, as they are sustanined even for time$= 400s$ of stimulation.

4.3 Travelling Wave Analysis of Brusselator

In the travelling wave analysis of the brusselator reaction diffusion PDE, unitary diffusion was assumed: $D_1 = D_2 = 1$. Introduction of the travelling wave coordinate $\xi = x + ct$ reduced the system to a $4 - dimensional$ travelling wave ODE:

$$\frac{d\phi}{d\xi} = \alpha \tag{4.1}$$

$$\frac{d\alpha}{d\xi} = \alpha c - A - \phi^2\psi + \phi(B+1) \tag{4.2}$$

$$\frac{d\psi}{d\xi} = \beta \tag{4.3}$$

$$\frac{d\beta}{d\xi} = \beta c - B\phi + \phi^2\psi \tag{4.4}$$

The Jacobian of the system was evaluated at the fixed point $(\phi, \alpha, \psi, \beta) = (A, 0, B/A, 0)$:

$$J_{fixedpoint} = \begin{pmatrix} 0 & 1 & 0 & 0 \\ 1-B & c & -A^2 & 0 \\ 0 & 0 & 0 & 1 \\ B & 0 & A^2 & c \end{pmatrix} \tag{4.5}$$

The determinant of the Jacobian is:

$$det \begin{pmatrix} -\lambda & 1 & 0 & 0 \\ 1-B & c-\lambda & -A^2 & 0 \\ 0 & 0 & -\lambda & 1 \\ B & 0 & A^2 & c-\lambda \end{pmatrix} \tag{4.6}$$

The method of *minors and cofactors* expands out the determinant of the Jacobian, and we choose to expand the matrix along its first row:

$$-\lambda \begin{vmatrix} c-\lambda & -A^2 & 0 \\ 0 & -\lambda & 1 \\ 0 & A^2 & c-\lambda \end{vmatrix} - 1 \begin{vmatrix} 1-B & -A^2 & 0 \\ 0 & -\lambda & 1 \\ B & A^2 & c-\lambda \end{vmatrix} \tag{4.7}$$

On further expansion:

$$-\lambda(c-\lambda)(-\lambda c + \lambda^2 - A^2) - [(1-B)(-\lambda c + \lambda^2 - A^2) - A^2 B] \tag{4.8}$$

Grouping together the common powers of λ, we arrive at the characteristic quartic equation:

$$\lambda^4 - 2c\lambda^3 + \lambda^2(c^2 - A^2 - 1 + B) + \lambda(cA^2 + c - Bc) + A^2 = 0 \tag{4.9}$$

The solution to a quartic requires reduction to depressed quartic form and solving of a cubic by the use of Cardano's method (refer to appendix for full method). Because of the number of algebraic steps involved in solving the quartic using this method, attempting to classify the nature of our fixed point becomes rather complex. A far more efficient alternative is to factor out the

$\lambda(\lambda - c)$ term in equation (4.8) to obtain a quadratic in terms of $\lambda(\lambda - c)$, and carry out a completion of the square on this quadratic, from which we obtain:

$$\lambda = \frac{c}{2} \pm \sqrt{\frac{c^2}{4} + \frac{A^2 + 1 - B}{2} \pm \sqrt{\left(\frac{A^2 + 1 - B}{2}\right)^2 - A^2}} \tag{4.10}$$

Now let:

$$T_1 = \frac{A^2 + 1 - B}{2}, T_2 = \left(\frac{A^2 + 1 - B}{2}\right)^2 - A^2 \tag{4.11}$$

So that we may express λ as:

$$\lambda = \frac{c}{2} \pm \sqrt{\frac{c^2}{4} + T_1 \pm \sqrt{T_2}} \tag{4.12}$$

Fixing the values of A and B to be $B = 3$ and $A = 1$ and leaving c to be a free parameter, we are interested in the bifurcation point at which the eigenvalues cross the Real-Imaginary axis. That is, the point where $\lambda = \pm i\omega$. With algebraic evaluation we found that this point occurs at $c = \sqrt{3/2} \approx 1.22$.

We start by equating λ to $\lambda = \pm i\omega$, so that (4.12) becomes:

$$\pm i\omega = \frac{c}{2} \pm \sqrt{\frac{c^2}{4} + T_1 \pm \sqrt{T_2}} \tag{4.13}$$

From which we can equate T_1 and T_2:

$$T_1 = -\omega^2, T_2^{1/2} = \pm i\omega c \tag{4.14}$$

Which after substituting T_1 and T_2 back in gives:

$$-\omega^2 c^2 = \left(\frac{A^2 + 1 - B}{2}\right)^2 - A^2 \tag{4.15}$$

$$-\omega^2 = \frac{A^2 + 1 - B}{2} \tag{4.16}$$

With the values of A=1 and B=3 we have set, the value of c satisfying equations (4.15) and (4.16) is therefore $c = \sqrt{(3/2)} \approx 1.22$. This is the critical value of c at the bifurcation point and we find that it is indeed consistent with the eigenvalue plot of figure 4.8. As figure 4.8 shows, a stable spiral in the 4-dimensional phase space bifurcates into an unstable spiral, suggesting that a Hopf bifurcation takes place as c is varied. The periodic orbit of a Hopf bifurcation suggests that we ought to observe periodic wave train solutions in our numerical results, but we have not observed these waves. We believe that we have yet to investigate the behaviour of the Brusselator over a larger range of values for the parameters A, B, D_1 and D_2 in order to obtain periodic wavetrains.

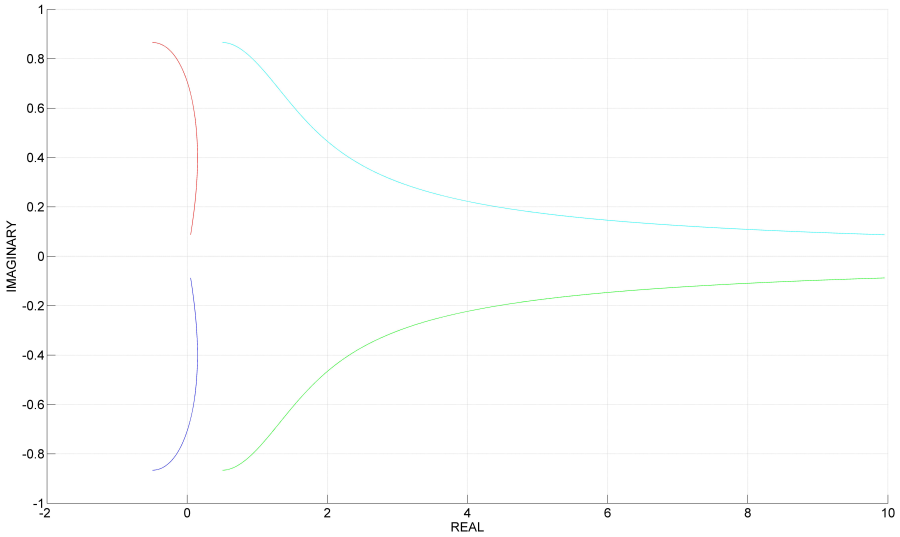

Figure 4.8: Plot of how the eigenvalues of the Brusselator travelling wave ODE vary as c(wavespeed) is varied from c= 0 to c= 10. There are initially a complex pair of eigenvalues (red and blue corresponds to ϕ and ψ) with negative real parts, indicating a stable spiral of the 4 dimensional phase space. A bifurcation point occurs at c$\approx$ 1.22 at which the negative eigenvalues become positive: a stable spiral bifurcating into an unstable spiral.

4.4 Turing Analysis of the Reaction Diffusion Mechanism

(Murray J.D., 1989). In a Turing instability, or diffusion driven instability, a system without diffusion remains stable when it is subjected to small perturbations. However, in the presence of diffusion, the system becomes unstable to small spatial perturbations.

Since we suspect that such diffusion driven instabilities occur in our system, we have to take this into account when performing our mathematical analysis. That is, the analysis is divided into two parts: in the first of these, the spatial dependency is removed from the Brusselator PDE, $D_1, D_2 = 0$, allowing us to derive the specific conditions required for stability to occur in a spatially independent case. These conditions are imposed throughout the second part of the analysis, when spatially dependency is allowed.

Before we begin the process of analysis for our reaction diffusion system, we have to bear in mind that there are in total, 4 parameters which can be varied: D_1, D_2, B and A. And that we have a single fixed point at $\phi_0, \psi_0 = (A, B/A)$. It is more convenient algebraically to not evaluate the steps during the analysis with a specific fixed point, but rather to specify the fixed point only after we derive the conditions for stability or instability at the end. The fixed point is such that A=1, without loss of generality, so $\phi_0, \psi_0 = (1, B)$.

We begin as mentioned above, by a removal of the spatial dependency:

$$\frac{d\phi}{dt} = A + \phi^2\psi - \phi(B+1) \tag{4.17}$$

$$\frac{d\psi}{dt} = B\phi - \phi^2\psi \tag{4.18}$$

Taking a perturbation about the fixed point ϕ_0 and ψ_0

$$\underline{w} = \begin{pmatrix} \phi - \phi_0 \\ \psi - \psi_0 \end{pmatrix} = \begin{pmatrix} u \\ v \end{pmatrix} \tag{4.19}$$

Use of the Taylor expansion to linearise system at our fixed point. For algebraic conviennience, we shall not evaluate the partial derivative terms for a specific fixed point just yet.

$$(\phi - \phi_0)_t = (\phi - \phi_0)\left.\frac{\partial f}{\partial \phi}\right|_{(\phi_0,\psi_0)} + (\psi - \psi_0)\left.\frac{\partial f}{\partial \psi}\right|_{(\phi_0,\psi_0)} + O(u^2, v^2, uv) \tag{4.20}$$

$$(\psi - \psi_0)_t = (\phi - \phi_0)\left.\frac{\partial g}{\partial \phi}\right|_{(\phi_0,\psi_0)} + (\psi - \psi_0)\left.\frac{\partial g}{\partial \psi}\right|_{(\phi_0,\psi_0)} + O(u^2, v^2, uv) \tag{4.21}$$

Neglecting the non-linear terms of equations (6 and 7) and expressing the

system in terms of u and v.

$$u_t = u\frac{\partial f}{\partial \phi} + v\frac{\partial f}{\partial \psi}$$
$$v_t = u\frac{\partial g}{\partial \phi} + v\frac{\partial g}{\partial \psi}$$

Expressed in terms of vector matrix notation.

$$\underline{w}_t = \begin{pmatrix} f_\phi & f_\psi \\ g_\phi & g_\psi \end{pmatrix} \begin{pmatrix} u \\ v \end{pmatrix} \tag{4.22}$$

Rewritten in compact notation as

$$\underline{w}_t = \underline{\underline{A}} * \underline{w} \tag{4.23}$$

We are now ready to determine the characteristic equation.

$$det(\underline{\underline{A}} - \lambda I) = 0 \tag{4.24}$$

$$det\left[\begin{pmatrix} f_\phi & f_\psi \\ g_\phi & g_\psi \end{pmatrix} - \begin{pmatrix} \lambda & 0 \\ 0 & \lambda \end{pmatrix}\right] = 0 \tag{4.25}$$

We arrive at the quadratic characteristic equation, still expressed in terms of the generic terms $f_\phi, f_\psi, g_\phi, g_\psi$, which remember, are to be evaluated for a particular fixed point.

$$\lambda^2 - \lambda(f_\phi + g_\psi) + f_\phi g_\psi - f_\psi g_\phi = 0 \tag{4.26}$$

It follows that the two conditions necessary for stability to occur ($Re(\lambda) < 0$) are:

$$f_\phi + g_\psi < 0 \tag{4.27}$$

$$f_\phi g_\psi - f_\psi g_\phi > 0 \tag{4.28}$$

For the specific fixed point mentioned above, $\phi_0, \psi_0 = (1, B)$, an evaluation of the derivatives f and g give: $f_\phi = B - 1, f_\psi = 1, g_\phi = -B, g_\psi = -1$. Looking at the 2 conditions for $Re(\lambda) < 0$, it is clear that (4.28) is always satisfied for any value of B. And condition (4.27) implies a further condition that $B < 2$. We now bring back the spatially dependence to our problem, so that:

$$\frac{\partial \phi}{\partial t} = D_1\frac{\partial^2 \phi}{\partial^2 x} + A + \phi^2\psi - \phi(B+1) \tag{4.29}$$

$$\frac{\partial \psi}{\partial t} = D_2\frac{\partial^2 \psi}{\partial^2 x} + B\phi - \phi^2\psi \tag{4.30}$$

Standard use of Taylor expansion, similar to previously.

$$(\phi - \phi_0)_t = D_1(\phi - \phi_0)_{xx} + (\phi - \phi_0)\frac{\partial f}{\partial \phi} + (\psi - \psi_0)\frac{\partial f}{\partial \psi} \tag{4.31}$$

$$(\psi - \psi_0)_t = D_2(\psi - \psi_0)_{xx} + (\phi - \phi_0)\frac{\partial g}{\partial \phi} + (\psi - \psi_0)\frac{\partial g}{\partial \psi} \tag{4.32}$$

Express in vector matrix notation.

$$\underline{w}_t = \begin{pmatrix} D_1 & 0 \\ 0 & D_2 \end{pmatrix} \begin{pmatrix} \nabla^2 u \\ \nabla^2 v \end{pmatrix} + \begin{pmatrix} f_\phi & f_\psi \\ g_\phi & g_\psi \end{pmatrix} \begin{pmatrix} u \\ v \end{pmatrix} \tag{4.33}$$

Express in a more compact notation.

$$\underline{w}_t = \underline{\underline{D}}\nabla^2 \underline{w} + \underline{\underline{A}} * \underline{w} \tag{4.34}$$

We are dealing with a bounded domain, such that the system is that of a closed one. This naturally dictates that we impose no flux boundary conditions.

$$(\underline{n} \cdot \nabla)\underline{w} = 0 \tag{4.35}$$

$\underline{n}$: unit normal to closed boundary of the domain. We hereby introduce the use of eigenfunctions in solving the problem. Specifically for our boundary conditions, the eigenfunction is:

$$\underline{w}_k = cos\left(\frac{n\pi x}{a}\right) \tag{4.36}$$

$\underline{w}_k$: the eigenfunction corresponding to the wavenumber k, where the wavenumber is: $k = (n\pi/a)$. On differentiating the eigenfunction:

$$\nabla^2 \underline{w}_k = -k^2 \underline{w}_k \tag{4.37}$$

Note that this is a linear problem and we look for solutions to equation (4.37) of the form:

$$\underline{w}(\underline{r}, t) = \Sigma C_k e^{\lambda t} \underline{w}_k(\underline{r}) \tag{4.38}$$

$\underline{r}$: spatial domain vector.
Substitution of this form into equation (4.37) gives:

$$\lambda \underline{w}_k(\underline{r}) = (\underline{\underline{A}} - \underline{\underline{D}}k^2)\underline{w}_k(\underline{r}) \tag{4.39}$$

From which we can proceed to find the characteristic quadratic for λ in the usual manner.

$$det[(\underline{\underline{A}} - \underline{\underline{D}}k^2) - (\lambda I)] = 0 \tag{4.40}$$

$$\lambda^2 + \lambda(-f_\phi + D_1k^2 - g_\psi + D_2k^2) + f_\phi g_\psi - D_2k^2 f_\phi - D_1k^2 g_\psi + D_1D_2k^4 - f_\psi g_\phi = 0 \tag{4.41}$$

For notational convennience

$$\lambda^2 + \lambda(\alpha) + \beta = 0 \tag{4.42}$$

For diffusion driven instability to occur, $Re(\lambda) > 0$ must hold. There are two ways in which this can be true: either $\alpha < 0$ or $\beta < 0$. From the conditions that we have derived above, we can prove that $\alpha < 0$ cannot be true. Consider $\alpha = -f_\phi + D_1k^2 - g_\psi + D_2k^2 < 0$, which with our fixed point, works out as

$2 + k^2(D_1 + D_2) < B$. But $B < 2$ as above, so $\alpha < 0$ is untrue.

So the only possible way for $Re(\lambda) > 0$ is if $\beta < 0$. That is,
$f_\phi g_\psi - D_2 k^2 f_\phi - D_1 k^2 g_\psi + D_1 D_2 k^4 - f_\psi g_\phi < 0$. Or, rearranged:

$$f_\phi g_\psi - f_\psi g_\phi + D_1 D_2 k^4 - k^2(D_2 f_\phi + D_1 g_\psi) < 0. \tag{4.43}$$

We know $f_\phi g_\psi - f_\psi g_\phi > 0$ from above, and it is clear that $D_1 D_2 k^4$ is always positive. So the only way for $\beta < 0$ is if $(D_2 f_\phi + D_1 g_\psi) > 0$. Which, with our fixed point is $D_2(B-1) > D_1$. With $B < 2$, a condition for diffusion driven instability is $D_2 > D_1$.

Further, on substitution of the fixed points into inequality (4.43), it reduces to $A^2 + D_1 D_2 k^4 < k^2(D_2(B-1) + D_1(-A^2))$. If we assume $D_1 = 0$, the final condition for diffusion driven instability is:

$$k > \sqrt{\frac{A^2}{D_2(B-1)}} \tag{4.44}$$

For the specific values $D_2 = 0.02$, $B = 1.5$, $A = 1$, we find that diffusion driven instabilities occur beyond the critical wavenumber $k = 10$, which is consistent with the plot shown in figure 4.9. This consolidates our numerical findings of section 4.2, as a finite value of $D_2 = 0.02$ and $D_1 = 0$ here generates a steady state, spatially heterogeneous solution. Further, if $D_1 = 0$ and $D_2 = 0$, a diffusion driven instability would not be possible, and we can see that from equation 4.43, where $f_\phi g_\psi - f_\psi g_\phi > 0$ has to be true. Since there is no diffusion driven instability when $D_1 = 0$ and $D_2 = 0$, spatially heterogeneous cannot exist, consistent with our numerical results.

4.5 Spatio-temporal Patterns in the Goldbeter

We have obtained numerical results for the Goldbeter et al. (1990) system by applying a piecewise β spatial profile (an example is given in figure 4.11) for the duration of the simulation. As figure 4.11 shows, there is a central oscillatory region in the profile where β is set such that the system oscillates, and it is surrounded by spatial regions where $\beta = 0.27$ (steady state solutions). A set of experiments were performed where different piecewise profiles were applied, the profiles all have different β levels for the oscillatory region, but the surrounding regions remain at $\beta = 0.27$ as before. We found that for sufficiently high levels of β we see unexpected oscillatory patterns as shown in figure 4.10, but for low β values, results are as we had anticipated (figure 4.12). As figure 4.12 shows, an agonist concentration of $\beta = 0.30$ applied to a region of the spatial domain generates an oscillatory region. This oscillatory region has the ability to elicit fully regenerative travelling waves. We believe that the waves propagate using the calcium induced calcium release mechanism. For the oscillatory region, an elevated calcium concentration is present whenever there is an oscillatory peak, and this rise in calcium diffuses through to the neighbouring regions to stimulate the CICR mechanism. Applying a sufficiently high β value of $\beta = 0.70$ instead of $\beta = 0.30$ to the same region under the same conditions however, produces different results. In

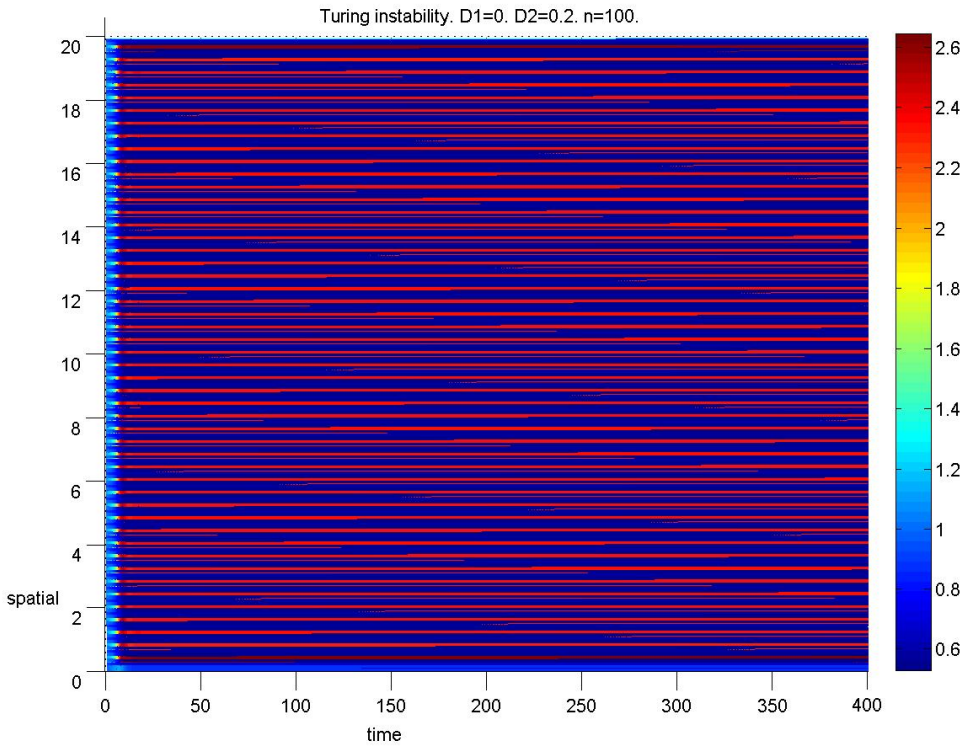

Figure 4.9: Numerical solutions to ϕ for $D_1 = 0$ and $D_2 = 0.02$ and wavenumber $k \simeq 15$ ($> criticalk = 10$). Spatially non-uniform patterns appear spontaneously.

figure (4.10), the system was first allowed to evolve to a steady state by applying to it a non-oscillatory value of $\beta = 0.27$, then a spatial agonist profile (as shown in figure 4.11) which contains an elevated region of $\beta = 0.70$ was applied for the remainder of simulation time. As figure (4.10) shows, we still observe an oscillatory region, but the region elicits a series of fully regenerative waves, semi-regenerative waves and a refractory period can also be observed where the oscillatory region fails to elicit any propagating waves at all.

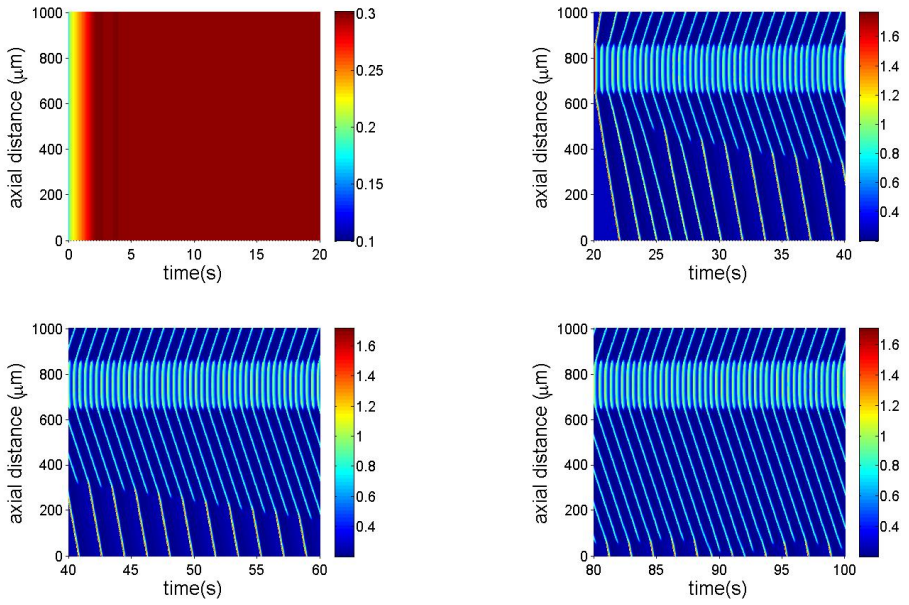

Figure 4.10: Figure shows the spatial-time plots for the concentration of cytosolic Ca^{2+} for four different time intervals, (A):$0-20s$, (B): $20s-40s$, (C):$40s-60s$, (D):$80s - 100s$. The β variation profile (figure 4.11) is only applied for time intervals (B)-(D). For the initial $20s$, $\beta = 0.27$ to allow for a transient evolution of the system to a steady state. As shown on graphs (A)-(D), there is an oscillatory region along the spatial domain which is capable of eliciting propagating waves. However, not every propagating wave behaves the same way: some waves are fully regenerative, while some waves are only semi-regenerative, in that they cease propagating after a certain time. We can also observe that on certain occasions, the oscillatory region fails to elicit a propagating wave, and we believe this to be due to a refractory period.

4.6 Comparison of Results

To date, there have been two CICR based discrete models developed, which may possibly be appropriate for use as a benchmark for our homogenised Goldbeter et al. (1990) results. The two models are Shaikh et al. (2012) and

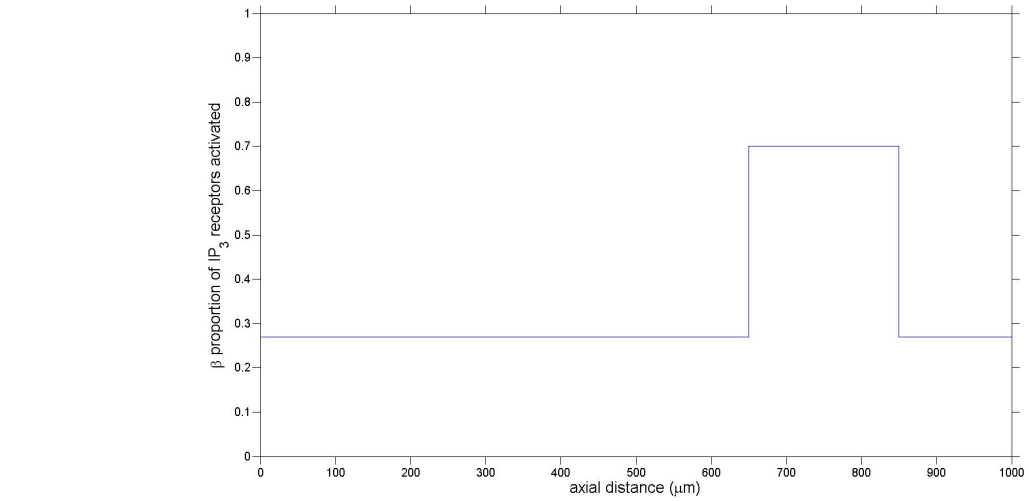

Figure 4.11: Spatial profile of how parameter β the level of activation of IP_3 receptor, varies along axial distance. There are 3 distinct regions: $\beta = 0.70$ and $\beta = 0.27$ on either side, $\beta = 0.70$ corresponds to an oscillatory region and $\beta = 0.27$ to a stable non-oscillatory steady state region.

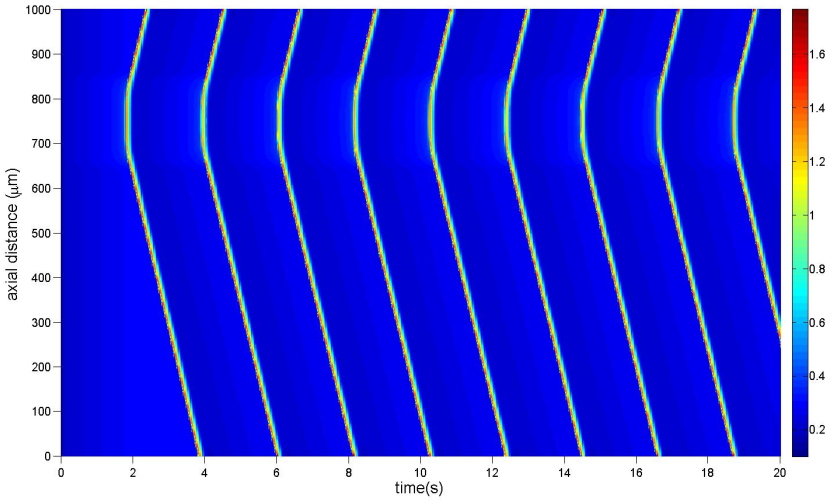

Figure 4.12: Spatial-time plot of the concentration of cytosolic Ca^{2+}. Along the spatial domain it is subjected to a similar β variation profile of figure (4.11), except $\beta = 0.30$ for the oscillatory region. Contrary to 4.10, propagating waves are formed from every oscillatory peak of the elevated β region.

Koenigsberger et al. (2010). As explained below, the experimental tests carried out by Koenigsberger et al. (2010) are not physiologically relevant to what we need to benchmark, so we informed Shaikh et al. (2012) of our specific needs and they produced a space-time graph (using their model), specifically for our purposes.

The rat mesenteric smooth muscle cell model of Koenigsberger et al. (2010) consists of an endothelium denuded SMC strip of discrete cells. Koenigsberger et al. (2010) showed that their model was able to reproduce the observations seen in experimental results. The discrete cells are coupled to each other electrically, but not through Ca^{2+} or IP_3. This is the crucial factor why the comparison of Koenigsberger et al. (2010) with Goldbeter et al. (1990) would not be a valid comparison. The Goldbeter et al. (1990) only assumes Ca^{2+} coupling. Nonetheless Koenigsberger et al. (2010) demonstrated that when an SMC strip is locally stimulated with phenylephrine agonist, a travelling wave of Ca^{2+} propagates along the SMC strip with a velocity which corresponds to the experimental velocity of $100\mu m s^{-1}$. This wave has a limited range of $400\mu m$ again in good agreement with experiments.

In their original paper, Shaikh et al. (2012) performed experiments on a bilayer structure consisting of a monolayer of discrete SMCs coupled with a monolayer of ECs on top. The discrete cells were coupled to each other through Ca^{2+}, IP_3 and electric potential. Their main result was that of a travelling wave of Ca^{2+} along the vessel. However following a discussion with Shaikh et al. (2012), the author was able to adapt their model such that the endothelial cell layer was made redundant and only Ca^{2+} coupling was present (IP_3 and electrical coupling were switched off). This makes for a valid comparison with our Goldbeter et al. (1990) model in that our system only assumes a line of cells coupled via Ca^{2+} only. Shaikh et al. (2012) applied a piecewise spatial agonist profile (as shown in figure 4.13) to a $13312\mu m$ length of SMCs, a very similar scenario to what we had for our experiment (figure 4.10). The region of the piecewise profile ($4576\mu m - 8944\mu m$) corresponding to $J_{PLC} = 0.85$ elicits a band of oscillatory calcium solutions in the population of SMCs. However even with the presence of diffusion, where the SMC-SMC gap-junctional permeability was set to $0.05s^{-1}$ (this was an assumed value, as no experimental data was available), no propagating waves of any kind can be observed to propagate out from this oscillatory band. This is in contrast to our results from Goldbeter et al. (1990) (figure 4.10), where the oscillatory band was capable of inducing a series of regenerative and semi-regenerative travelling waves in its neighbouring cells. Therefore our results suggest that Goldbeter et al. (1990) contains the necessary mechanism required for generation of calcium oscillations, but it does not have the sufficient conditions required to completely reproduce the physiological results of Shaikh et al. (2012). Our model lacks the necessary complexity (inclusion of VOCCs, potassium channels (SK_{Ca})) as found in other physiological models. Specifically, our model does not include the membrane oscillator mechanism, which is vital because of its ability to trigger oscillations by eliciting the CICR mechanism. In their model, Shaikh et al. (2012) couples the membrane oscillator non-linearly with the CICR.

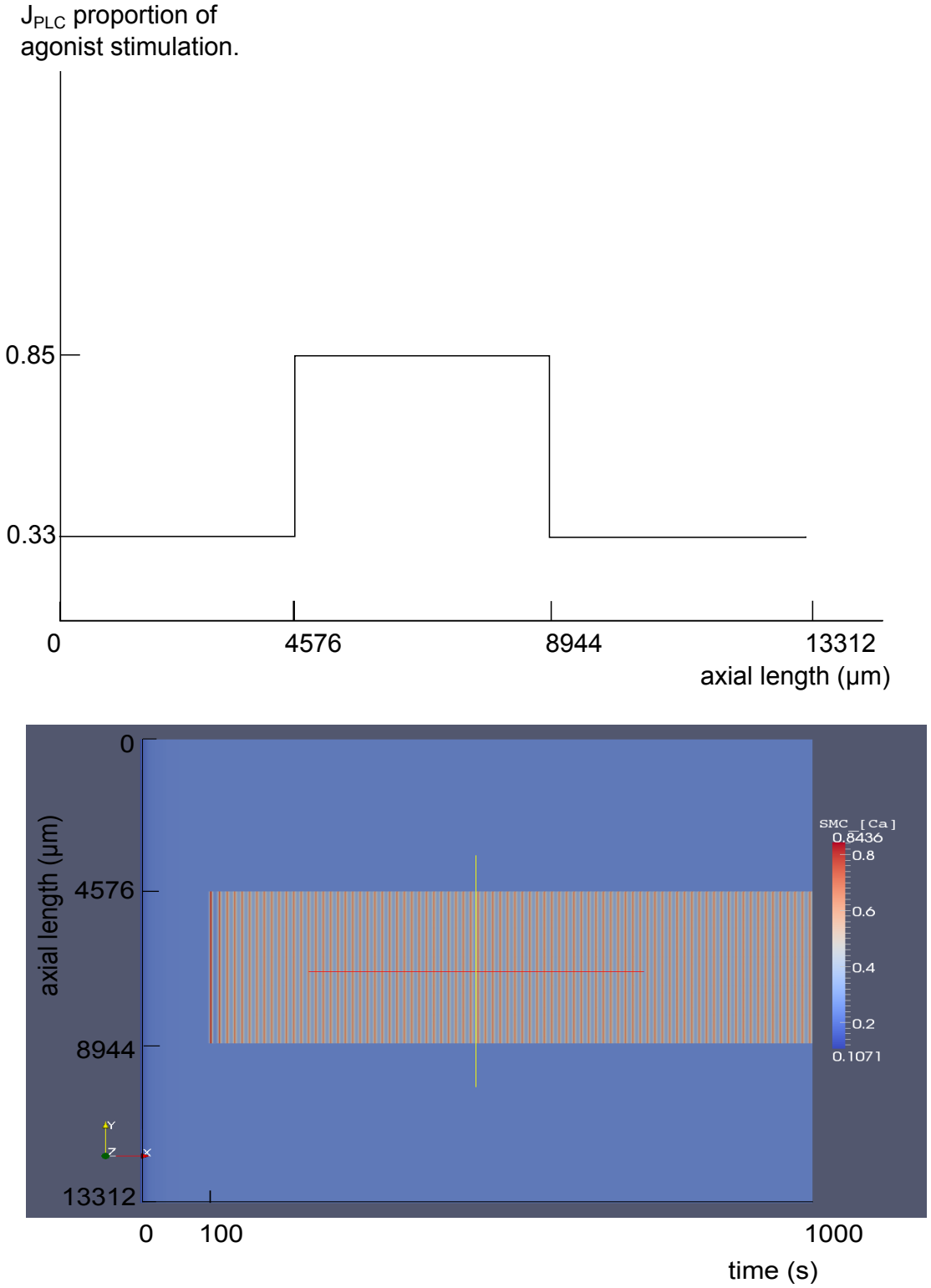

Figure 4.13: The results taken from Shaikh et al. (2012) system. A piecewise agonist profile is applied to a monolayer segment of SMCs of length $13312\mu m$. The spatio-temporal graph shows how the SMC calcium concentration of this segment of SMCs evolve as it is subjected to the piecewise profile. The agonist profile was applied only after 100 seconds of simulation time, so as to account for any transient effects and allow the system to settle to a steady state first. As shown there is an oscillatory region ($4576 - 8944\mu m$), but this region fails to elicit any propagating waves in the neighbouring regions.

4.7 Travelling Wave Analysis

Given the physiological parameter values, and setting $\beta = 0.27$ the 3 fixed points of the reaction ODE system are (using $Maple^{\text{TM}}$ software): $(Y = 2.1400, Z = 0.2971), (Y = -1.3679 + 2.8255 * I, Z = 0.2971), (Y = -1.3679 - 2.8255 * I, Z = 0.2971)$ of which only the positive, real fixed point $(Y = 2.1400, Z = 0.2971)$ is physiological. After introducing the travelling wave coordinate $\xi = x + ct$, the travelling wave ODE system is:

$$\frac{dZ}{d\xi} = \alpha \tag{4.45}$$

$$\frac{d\alpha}{d\xi} = \frac{1}{D}\left(\alpha c - v_0 - v_1\beta + v_2 - v_3 - k_f Y + kZ\right) \tag{4.46}$$

$$\frac{dY}{d\xi} = \frac{1}{c}\left(v_2 - v_3 - k_f Y\right) \tag{4.47}$$

The physiological steady state for the travelling wave system is $\mathbf{fp} = (Y = 2.1400, \alpha = 0, Z = 0.2971)$, from which we can analyse its local linear stability. The characteristic cubic polynomial of the system can be found by evaluating its Jacobian at the fixed point. This was done using $Maple^{\text{TM}}$, and a singularity was found to occur at $c = 0$, as shown in 4.48. Although $Maple^{\text{TM}}$ was capable of finding eigenvalues for specific fixed points, it proved ineffective in obtaining $3 - dimensional$ plots of c(wavespeed) against the Imaginary and Real parts of the eigenvalues. Therefore $Matlab^{\text{TM}}$ was used to numerically estimate the eigenvalues of the system for a range of different values for c(wavespeed), figure 4.14. Figure 4.14 shows that there exists a pair of stable complex eigenvalues and one unstable purely real eigenvalue for the parameter space $\beta = 0.27$, suggesting a homoclinic orbit. And a homoclinic orbit is indeed what we obtain from our numerical results as well, as shown in figure 4.17. Therefore since our travelling wave analysis is consistent with our numerical findings, we have a strong argument that travelling pulse waves exist in the homogenised Goldbeter et al. (1990).

A set experiments were performed for β spatial profiles held only for the initial $1s$ of the simulation (figure 4.16 is an example), which generates a single travelling pulse from which the homoclinic orbit of the pulse could be extrapolated (figure 4.17). The wavespeeds of these travelling pulses were estimated for a range of different diffusion values, and figure 4.18 shows the relationship.

Set of experiments performed in which one particular parameter value of the system (either $v_0, kor V_{M2}$) had a spatially non-uniform piecewise profile, while all other parameters were spatially uniform. This was to investigate the ability of certain parameters to elicit travelling waves. Authors suggested that for sufficiently large values of v_0 or sufficiently low k, oscillations can develop spontaneously. Our experiments have consistently shown that v_0 and k were capable of eliciting travelling waves. Varying V_{M2} however, had no effect.

$$-\frac{-0.00070\lambda c + (1/500)\lambda^2 c^2 - 2.724\lambda^2 - \lambda^3 c + 0.0545}{c} \tag{4.48}$$

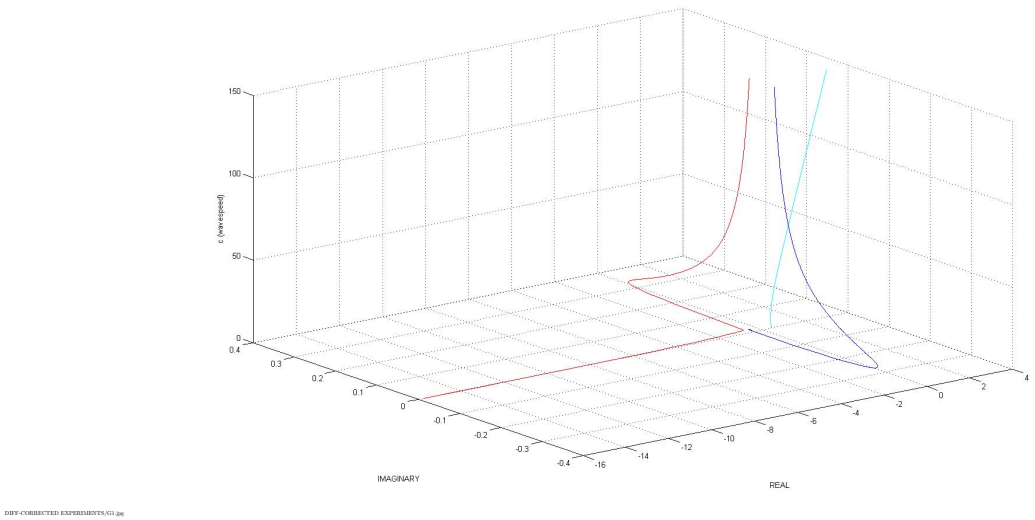

DIFF-CORRECTED EXPERIMENTS/G1.jpg

Figure 4.14: Plot shows how the 3 eigenvalues of equation 4.48 (coloured red, blue, cyan) vary for a range of values for c(wavespeed). Its corresponding $2-$ *dimensional* Real-Imaginary plot is shown in figure 4.15. There exists a pair of stable complex eigenvalues (red and blue) and one unstable purely Real eigenvalue (cyan).

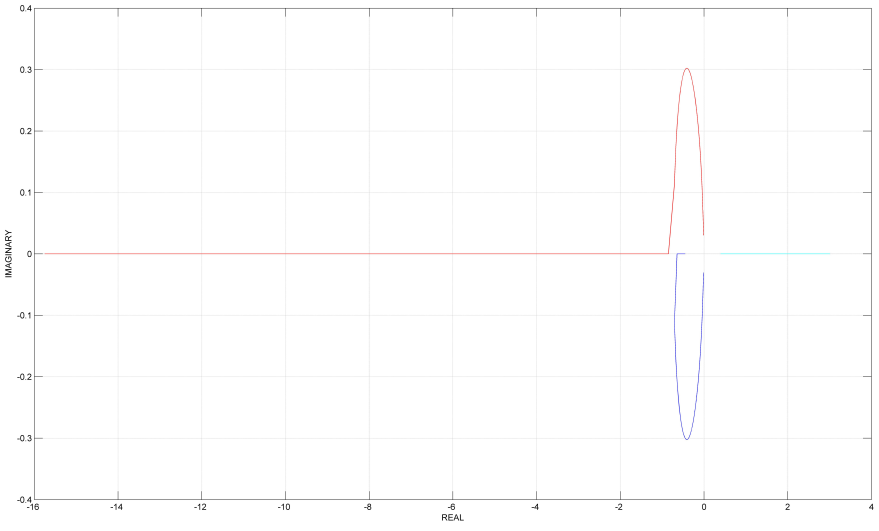

Figure 4.15: The $2-$ *dimensional* Real-Imaginary plot of figure 4.14.

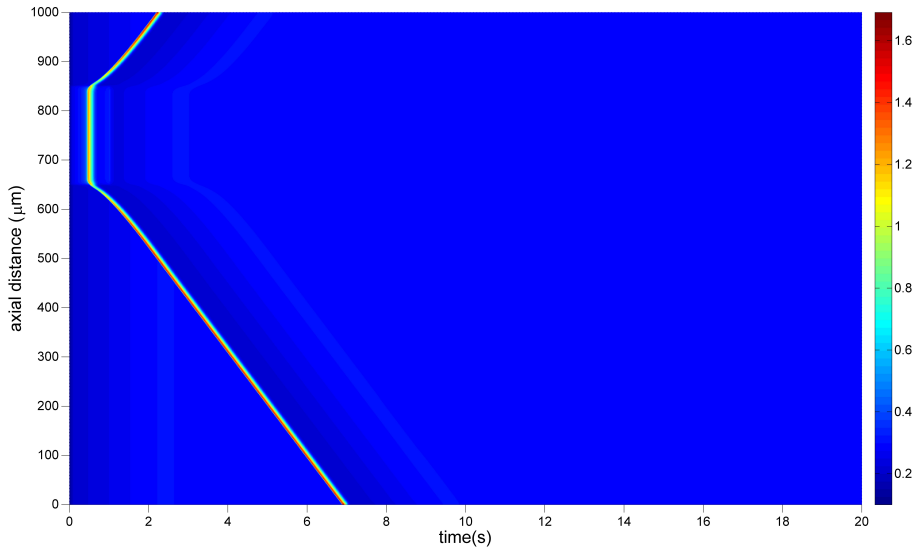

Figure 4.16: A similar spatial β profile to that of 4.11 (except that $\beta = 0.50$) was applied for an initial $1s$ to generate a single propagating wave. The estimated speed of the wave is $\approx 110\mu ms^{-1}$

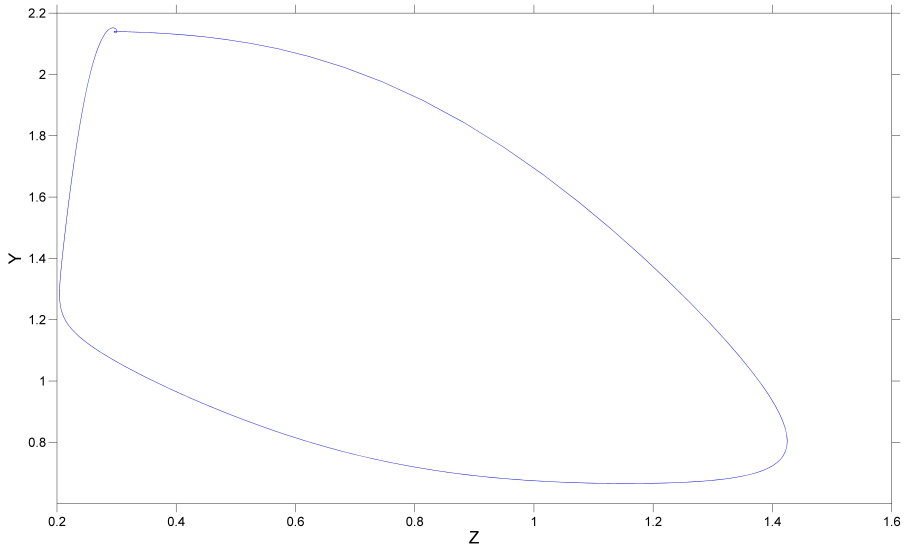

Figure 4.17: A plot of the homoclinic orbit obtained by measuring the numerical values of the cytosolic Ca^{2+} concentration and SR Ca^{2+} concentration of the system in figure 4.16 for time= $6s$.

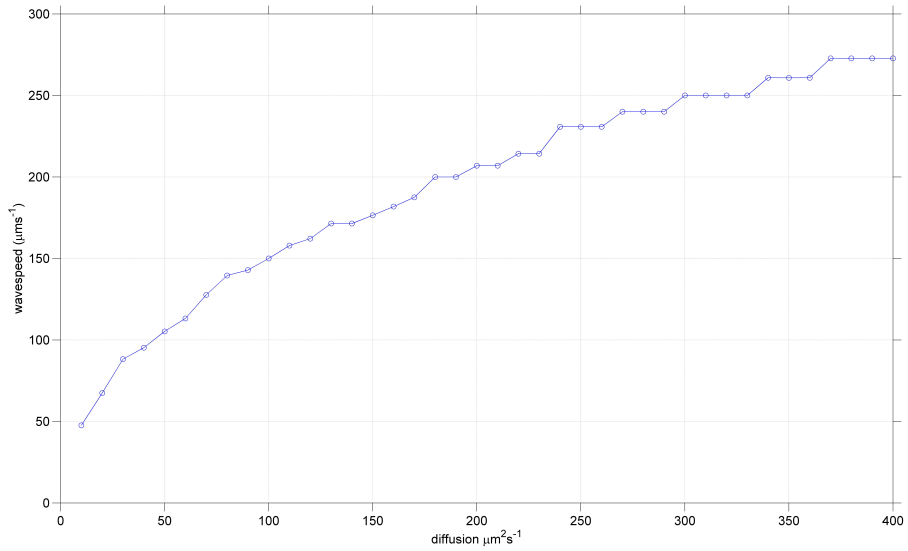

Figure 4.18: Plot shows how the wavespeed ($\mu m s^{-1}$) of a propagating wave increases with increasing values of the diffusion coefficient, D ($\mu m^2 s^{-1}$). As shown, wavespeed increases in a logarithmic fashion with increasing diffusion strength, with the greatest increase in wavespeed at diffusion $\lesssim 200 \mu m^2 s^{-1}$. The propagating wave was generated by applying a piecewise function for an initial time ($0-1s$). The piecewise function is similar to 4.11, but with $\beta = 0.30$ in the oscillatory region.

4.8 Discussion

We studied the theoretical Brusselator system extensively in the hope that it would give us a better understanding of oscillatory reaction diffusion systems in general, before we come to develop our realistic homogenised models. The ODE form of the Brusselator (without any spatial dimension) gives rise to oscillatory solutions if one of its parameters (parameter B) is increased beyond a critical value, but steady state solutions are observed if parameter B is below the threshold. Increasing parameter B increases the amplitude of oscillations, while at the same time decreases their frequency.

A spatial dimension was extended onto the Brusselator ODE to transform it into a PDE. The effects of diffusion on the behaviour of this Brusselator PDE were investigated: it was found that diffusion could synchronise oscillations along the length of the spatial domain. However, diffusion could also have an inhibitory effect on oscillations: if the system is displaying oscillatory spatio-temporal patterns, increasing diffusion can abolish these oscillatory patterns, forming steady state but spatially heterogeneous solutions. However we believe that a limitation of our experiments was that diffusion was not varied over a wide enough range of values, which could possibly explain why we could not observe periodic train waves. A mathematical analysis of the travelling wave ODE of the Brusselator suggests the existence of a Hopf bifurcation, and the limit cycle of the Hopf bifurcation suggests that we ought to be observing periodic wavetrain solutions for our numerical results. More investigation is therefore needed to complete our study. We have also determined the conditions required for diffusion driven instability to occur in the system.

We have developed the homogenised Goldbeter et al. (1990) model and we hoped that provided our results were in good agreement with those of the discrete Shaikh et al. (2012) model, this would prove the hypothesis that homogenised models can be used to generate the same results as their discrete counterparts. Our numerical results showed strong evidence for travelling wave phenomenon, but those of the discrete Shaikh et al. (2012) model did not. We believe this to be due to our model not having sufficient realism, in that it did not contain voltage operated calcium channels (VOCCs) and potassium channels K_{Ca}, the components responsible for the membrane oscillator mechanism.

Whilst physiologically, our Goldbeter et al. (1990) model and the model of Shaikh et al. (2012) are both based on the same calcium induced calcium release (CICR) mechanism to generate oscillations, Shaikh et al. (2012) has far more ion channels. Shaikh et al. (2012) incorporates the membrane potential oscillator into their system, which is a vital mechanism due to its ability to trigger oscillations in cells. The membrane oscillator consists of the small calcium activated potassium channels (SK_{Ca}), large calcium activated potassium channels (BK_{Ca}), voltage operated calcium channels (VOCCs), sodium chlorine exchanger (NaCl), and chlorine influx channel. All of these components were never included in our model (Goldbeter et al. (1990)). Of course, our interest is in how many of these components do we need to

incorporate into our model before our results fully agree with those of Shaikh et al. (2012). It may be that we only require the inclusion the VOOCs and (K_{Ca}) channels in our model to achieve this, or do we need to include every component that Shaikh et al. (2012) has included? This question is left for future work to answer, where the components may be introduced into our system in a separate manner, so that we may identify the critical component(s) responsible for producing the exact results as those of Shaikh et al. (2012). Another factor we need to consider is that of intercellular coupling. As we make our model more complex, we ought to account for membrane potential coupling and IP_3 coupling as well, since we believe that calcium coupling alone would not be able to produce propagating waves.

To consolidate our numerical results of travelling waves, a mathematical analysis of the travelling wave reduced ODE for Goldbeter et al. (1990) system was performed. That is, the characteristic eigenvalues for an appropriate fixed point of the ODE were analysed. The eigenvalues do indeed confirm the existence of a stable manifold (pair of negative complex eigenvalues) and an unstable manifold (a positive purely real eigenvalue). This is consistent with the homoclinic travelling wave orbit that was obtained from our numerical results.

4.9 Conclusions

The aim of this thesis was to prove that the homogenised modelling approach for a particular system can be used to replicate observations of the discrete modelling approach for the same system. We aimed to achieve this by deriving a homogenised model based on Goldbeter et al. (1990) and benchmarking its results with those of the discrete Shaikh et al. (2012), which have already been validated with experimental findings. Prior to starting work on Goldbeter et al. (1990), which is a reaction diffusion system, our goal was to model the Brusselator PDE, hoping that it would provide us with a better understanding of reaction diffusion systems in general.

So far, our model of Goldbeter et al. (1990) has the necessary components to generate oscillatory behaviours and travelling waves, but we believe that it lacks the sufficient cell components for it to generate the exact results of Shaikh et al. (2012), which is what is required for the hypothesis to be proven. Given similar parameter conditions to Goldbeter et al. (1990), the results of Shaikh et al. (2012) do not show evidence of travelling waves, even though they show oscillatory behaviour. Our Goldbeter et al. (1990) system currently has the CICR mechanism accounted for, but it does not contain the ion channels of the membrane oscillator mechanism, namely calcium activated potassium channels K_{Ca}, voltage operated calcium channels (VOCCs), sodium chlorine exchanger (NaCl) and chlorine influx channel, therefore future work is required to identify specifically the channel(s) that are responsible for replicating the results of Shaikh et al. (2012). We may do this by incorporating the channels into our model in a separate basis, and study the behaviour that a particular channel has on the system. So although we have yet to prove our hypothesis, we have found that the CICR mechanism in the

homogenised Goldbeter et al. (1990) reaction diffusion PDE is capable of eliciting travelling wave phenomena, and we have consolidated this through travelling wave analysis of the system.

For the Brusselator PDE, again further work is required to fully understand the system. We have found that the two different diffusion parameters D_1 and D_2 of the system have very different effects on the behaviour of the solutions. Whilst increasing D_1 can synchronise oscillations along the spatial domain, essentially causing them to oscillate in phase with each other, increasing parameter D_2 can in fact abolish oscillations and generate a pattern of spatially non-homogeneous, steady state solutions. Such spatially inhomogeneous patterns are in fact Turing instabilities or 'diffusion driven instabilities', and we have mathematically derived the conditions for Turing instabilities to occur in our Turing analysis. Our Turing analysis do indeed agree with our numerical findings on the effect of D_2. The travelling wave analysis of Brusselator PDE suggests the existence of a Hopf bifurcation, and the periodic cycle of a Hopf bifurcation implies that periodic wavetrains ought to exist in Brusselator PDE. However we have yet to find such wavetrains in our numerical simulations, and we believe that we have not varied the values of our parameters, namely D_1, D_2, B, A over a wide enough range. This is left for future work.

Appendices

.1 Matlab Code

The namess of the programs I have used to generate the figures in this thesis are: (for Brusselator PDE): 'rough1', 'rough2', 'piecewise', '$Brussela\_final$'. (for Goldbeter): '$HEAVISIDE\_GOLDBETTER\_main$', '$HEAVISIDE\_GOLDBETTER\_PDE'$, 'HEAVISIDE', '$GOLDBETTER\_TWFINAL2\_RECOVER'$. A separate page exists for each program.

Note that 'rough1' is a main program that calls 'rough2' and 'piecewise'. Similarly, '$HEAVISIDE\_GOLDBETTER\_main$' is a main program that calls '$HEAVISIDE\_GOLDBETTER\_PDE'$ and 'HEAVISIDE'.

.2 Code for Brusselator PDE results

```
%{
PROGRAM NAME: 'rough1'
PROGRAM DESCRIPTION
This program solves the Brusselator PDE using the 'method of lines'. This
is the main program. The called functions are 'rough2.m' and 'piecewise.m'
%}

%USER INPUT
%{
*select your N and fx. For the spatial mesh.
*select your ft and tt. For the time mesh.
*select diffusion D1, and diffusion D2.
*make sure your spatial profile is correct in the calling
function 'piecewise.m'
%}

%command lines
%parameters
A = 1;
%USER INPUT
D1 = 2.8;
D2 = 22.4;
%USER INPUT
fx = 100;
N = 2000;


%USER INPUT
ft=100;
tt=2000;
t = linspace(0, ft, tt);

%setting up the spatial mesh
x = linspace(0, fx, N);

%setting up the spatial matrix 'M'. Used in the 'method of lines'.
v=[-1;repmat(-2,N-2,1);-1]; %a column of -1 and -2's. To be used for the main diagonal of
M=diag(v,0)+diag(ones(N-1,1),1)+diag(ones(N-1,1),-1); %refer to 'matlab notes' handwritten
M = sparse(M);
I = sparse(eye(N));
jpattern = spones([M, I; I, M]);

odefun = @(t, y) rough2(t, y, A, D1, D2, fx, N, M, x);


%Dealing with the solution
y0=[repmat(2,2*N,1)]; %setting up the initial conditions.
options = odeset('JPattern', jpattern);
```

```
tic
[t,y]=ode15s(odefun,t,y0, options);
toc


[T, X] = meshgrid(t, x);

y_t=[y.'];
phi=y_t(1:N,:);
mesh(T, X, phi);
colorbar;
view(2);
set(gca,'TickDir','out','FontSize',15)
ylabel('spatial','FontSize',15)
xlabel('time','FontSize',15)
```

```
%{
PROGRAM NAME: 'rough2'
PROGRAM DESCRIPTION
Program contains the Brusselator PDE system, discretised with the method of
lines. It calls the function 'piecewise.m'
%}


function [dy_dt]=rough2(t,y,A,D1,D2,fx,N, M, x);%,A,B,fx,NEQ,N,DS,D1,D2,spatial);
%x=[1;2;3;4;3;9];  %ignore this. Just used for debugging.

NEQ=2*N;
%x = linspace(0, fx, N);
B = piecewise(x);%note that B is outputted as a row vector. enter piecewise(x) for linear
B = B(:);
DS = fx/N;
%spatial=[0:DS:20-DS]; %the spatial mesh. for use in plotting the contour plot.

dy_dt=[(D1/(DS)^2).*(M*y(1:N))+A+((y(1:N)).^2).*y(N+1:NEQ)-(B+1).*(y(1:N));

(D2/(DS)^2).*(M*y(N+1:NEQ))+B.*(y(1:N))-(y(1:N).^2).*(y(N+1:NEQ))];
return

%command lines
%parameters
%ft=100;
%tt=2000;
%dt=ft/tt;
%fx=20;
%NEQ=100;
%N=NEQ/2;
%DS=fx/(N);


%setting up the spatial mesh
%spatial=[0:DS:20-DS];
%spatial_t=[spatial.'];
%spatial2=[repmat(spatial_t,1,tt)];

%setting up the time mesh
%t=[0:dt:ft-dt];
%t2=[repmat(t,N,1)];

%Dealing with the solution
%x0=[repmat(2,NEQ,1)];
%[t,x]=ode15s(@PDE_brusselnew2,t,x0);
%x_t=[x.'];
%phi=x_t(1:N,:);
%mesh(t2,spatial2,phi);
```

```
%{
PROGRAM NAME: 'piecewise'
PROGRAM DESCRIPTION
This calling function contains the spatially varying profile for parameter
B, for the Brusselator PDE system. 2 choices are available, you can either have a linear p
Copy and paste into the function as appropriate.
%}

function  b = piecewise(x)
fx=100;
b(find(x<=0.65*fx))=1.9;
b(find((0.65*fx)<x & x<=(0.85)*fx))=3;
b(find((0.85)*fx<x))=1.9;


%type these into the command window to see the shape of the graph.
%{
fx=1000;
N=10000;
x=linspace(0,fx,N);
y=piecewise(x);
plot(x,y)
%}

%This is the piecewise spatial profile. Copy and paste into function above
%to use.
%{
fx=1000;
b(find(x<=0.65*fx))=1.9;
b(find((0.65*fx)<x & x<=(0.85)*fx))=3;
b(find((0.85)*fx<x))=1.9;
%}

%{
%This is the linear spatial profile. Only suitable for spatial domain of
20. Copy and paste into function above to use.
% first range
x2=x(x<10); %all the values of vector x that are less than 10 are assigned to x2.
b(find(x < 10)) = 0.4*x2+1;
% fourth range
x3=x(10<=x); %all values of vector x greater or equal to 10 assigned to x3.
b(find(10 <= x)) = -0.4*x3+9; %'find' function finds the indices (not values) of the eleme
%}

%{
%This is the profile for turing instability. Only suitable for spatial domain of 20. Uncom
% first range
x2=x(x<10); %all the values of vector x that are less than 10 are assigned to x2.
b(find(x < 10)) = 1.5;
% fourth range
```

```
x3=x(10<=x); %all values of vector x greater or equal to 10 assigned to x3.
b(find(10 <= x)) = 1.5; %'find' function finds the indices (not values) of the elements gr
%}
```

```
PROGRAM NAME: 'Brussela_final'
%program plots the 4 eigenvalues of the fixed point of the Brusselator travelling wave sys
%It plots a 3D line plot where x,y,z axis are REAL, IMAGINARY,
%c(wavespeed).

%{
USER INPUT
*Select paramter B
*Select range of c(wavespeed) you wish to find the eigenvalues of.
*Enter the initial guess for the fixed point of the system given the parameters you have c
%}

%USER INPUT
B=3;
A=1;
%USER INPUT
c_FINAL=10; %define the range of c you want to vary over
c_START=0;
c_NUMPOINTS=1000; %define the step sizes you want to vary c with.
c_STEP=(c_FINAL-c_START)/c_NUMPOINTS;

for INDEX=1:c_NUMPOINTS
f=@(a) [a(2);a(2)*(INDEX*c_STEP)-A-(a(1))*(a(1))*a(3)+a(1)*(B+1);a(4);a(4)*(INDEX*c_STEP)-
%opts = optimset('TolFun', 1e-18);
%USER INPUT
[FIXEDPOINT,~,~,~,JACOBIAN] = fsolve(f, [0.9;0;2.9;0]);%If B=3, A=1 the fixed pts of syste
EIGENVALUES(:,INDEX)=eig(JACOBIAN);
end

EIGENVALUES; %EIGNEVALUES contains the 4 eigenvalues of the system (rows) for various diff
REAL=real(EIGENVALUES); %REAL contains only the real parts of EIGENVALUES.
IMAGINARY=imag(EIGENVALUES); %IMAGINARY contains only the imaginary parts of EIGENVALUES.

REAL1=REAL(1,:);
REAL1=REAL1.'; %REAL1 contains only the first row of REAL.
REAL2=REAL(2,:);
REAL2=REAL2.'; %REAL2 contains only the first row of REAL.
REAL3=REAL(3,:);
REAL3=REAL3.'; %REAL3 contains only the first row of REAL.
REAL4=REAL(4,:);
REAL4=REAL4.'; %REAL4 contains only the first row of REAL.

IMAGINARY1=IMAGINARY(1,:);
IMAGINARY1=IMAGINARY1.'; %IMAGAINARY1 contains only the first row of IMAGINARY.
IMAGINARY2=IMAGINARY(2,:);
IMAGINARY2=IMAGINARY2.'; %IMAGAINARY2 contains only the first row of IMAGINARY.
IMAGINARY3=IMAGINARY(3,:);
IMAGINARY3=IMAGINARY3.'; %IMAGAINARY3 contains only the first row of IMAGINARY.
IMAGINARY4=IMAGINARY(4,:);
IMAGINARY4=IMAGINARY4.'; %IMAGAINARY4 contains only the first row of IMAGINARY.
```

```
c_VALUES=linspace(c_START,c_FINAL,c_NUMPOINTS);%The range of values you want to vary param

FIXEDPOINT


plot3(REAL1,IMAGINARY1,c_VALUES,'r');
hold on
plot3(REAL2,IMAGINARY2,c_VALUES,'b');
hold on
plot3(REAL3,IMAGINARY3,c_VALUES,'c');
hold on
plot3(REAL4,IMAGINARY4,c_VALUES,'g');
hold off
set(gca,'FontSize',15)
xlabel('REAL','FontSize',15)
ylabel('IMAGINARY','FontSize',15)
zlabel('c (wavespeed)','FontSize',15)
grid on

%{
plot(REAL1,c_VALUES,'r');
grid on
%}
```

.3 Code for Goldbeter results

```
%{
PROGRAM NAME: 'HEAVISIDE_GOLDBETTER_main'
PROGRAM DESCRIPTION
Program finds solutions to the GOLDBETTER system while a spatially varying
profile for parameter BETA is applied. The spatial profile is in the form
of a piecewise function. This is the main function.
'HEAVISIDE_GOLDBETTER_PDE' and 'HEAVISIDE' are two calling functions that
are called. Main function also contains bits of code (commented out) to be used for obtain
homoclinic orbit trajectories for a particular snapshot in time of the solutions. Uncommen
as appropriate.
%}

%{
USER INPUT
*select your N and fx. For the spatial mesh.
*select your ft and tt. For the time mesh.
*select diffusion D1
*make sure your piecewise spatial profile is correct in the calling
function 'HEAVISIDE_GOLDBETTER_PDE'
*check if you want the piecewise profile to be held for just an initial 1 second or
for duration of simulation.
%}

%SYSTEM PARAMETERS
v_0=1;
v_1=7.3;
k=10;
k_f=1;
k_A=0.9;
k_R=2;
K_2=1;
m=2;
n=2;
p=4;
V_M2=65;
V_M3=500;
%USER INPUT
fx=1000;%spatial domain.
%USER INPUT
N=1000;%Number of discrete spatial points.
%USER INPUT
D1=50;%Diffusion coefficient.
D2=0;

%setting up the time mesh
%USER INPUT
ft=20;
tt=1000;%Number of discrete time points.
```

```
t=linspace(0,ft,tt);

%setting up the spatial mesh
x=linspace(0,fx,N);


%{
%Code below is for obtaining homoclinic trajectory.
%Code below is for working out the numerical estimate of the differential to
%dZ/dPSI. Will be used later to obtain the homoclinic orbit in phase plane. Uncomment to u
dia1_trav=[repmat(-1,N-1,1);0]; %the vector that is to be the main diagonal of the matrix.
dia2_trav=[repmat(1,N-1,1)];%the vector that is to be above the main diagonal.
dia3_trav=[repmat(0,N-1,1)];%the vector that is to be below the main diagonal.
M_trav=diag(dia1_trav,0)+diag(dia2_trav,1)+diag(dia3_trav,-1);%the spatial matrix.
M_trav=sparse(M_trav);
%}

%setting up the spatial matrix 'M'. Used in the 'method of lines'.
dia1=[-1;repmat(-2,N-2,1);-1]; %the vector that is to be the main diagonal of the matrix.
dia2=[1;repmat(1,N-2,1)];%the vector that is to be above the main diagonal.
dia3=[repmat(1,N-2,1);1];%the vector that is to be below the main diagonal.
M=diag(dia1,0)+diag(dia2,1)+diag(dia3,-1);%the spatial matrix.
M = sparse(M);%compress our sparse spatial matrix.
I = sparse(eye(N));
jpattern = spones([M, I; I, M]);

odefun=@(t,CONC) HEAVISIDE_GOLDBETTER_PDE(t,CONC,v_0,v_1,k,k_f,k_A,k_R,K_2,m,n,p,V_M2,V_M3

%these are the default initial conditions.

%setting up the initial conditions
INITIAL1=repmat(0.1,N,1);
INITIAL2=repmat(1.35,N,1);
CONC0=vertcat(INITIAL1,INITIAL2);


%uncomment this for spatially inhomogenous initial conditions
%{
INITIAL1a=repmat(0.1,0.65*N,1);
INITIAL1b=repmat(0.5,0.2*N,1);
INITIAL1c=repmat(0.1,0.15*N,1);
INITIAL1=vertcat(INITIAL1a,INITIAL1b,INITIAL1c);
INITIAL2=repmat(1.35,N,1);
CONC0=vertcat(INITIAL1,INITIAL2);
%}

opts = odeset('JPattern', jpattern);
tic
[t,CONC]=ode15s(odefun,t,CONC0,opts);
toc
```

```
%[T,X]=meshgrid(t(2000:3000),x); %meshgrid creates a matrix with rows as dimensions of spa
[T,X]=meshgrid(t,x);
CONC_transpose=[CONC.']; %note: CONC is a matrix.
%CYTO_CALCIUM=CONC_transpose(1:N,2000:3000); %for obtaining solutions for a
%particular interval in time.
CYTO_CALCIUM=CONC_transpose(1:N,:);%The solution matrix of cytosolic calcium concentration
CYTO_CALCIUM_Y=CONC_transpose(N+1:2*N,:);%The solution matrix of SR calcium concentration.
mesh(T,X,CYTO_CALCIUM);
colorbar;
view(2);
set(gca,'TickDir','out','FontSize',15)
xlabel('time(s)','FontSize',20)
ylabel('axial distance (\mum)','FontSize',20)

%{
%these are for obtaining homoclinic trajectories. They are snapshots in time of
%Z, Y, AND ALPHA, expressed as vectors. To be copied and pasted into
command window.
TRAV_VECTOR=CYTO_CALCIUM(:,300);%The solution of cytosolic calcium
concentration for a specific snapshot in time.
TRAV_VECTOR_Y=CYTO_CALCIUM_Y(:,300);%The solution of SR calcium
concentration for a specific snapshot in time.
TRAV_VECTOR_ALPHA=M_trav*TRAV_VECTOR;
plot3(TRAV_VECTOR,TRAV_VECTOR_ALPHA,TRAV_VECTOR_Y);
set(gca,'TickDir','out','FontSize',15)
xlabel('Z','FontSize',20)
ylabel('\alpha','FontSize',20)
zlabel('Y','FontSize',20)
TRAV_VECTOR(900,1)
TRAV_VECTOR_ALPHA(900,1)
TRAV_VECTOR_Y(900,1)
%}



%{
%these are for the travelling wave analysis. They are snapshots in time of
%Z, Y, AND ALPHA, expressed as vectors.
TRAV_VECTOR=CYTO_CALCIUM(:,100);
TRAV_VECTOR_Y=CYTO_CALCIUM_Y(:,100);
TRAV_VECTOR_ALPHA=M_trav*TRAV_VECTOR;
plot(TRAV_VECTOR,TRAV_VECTOR_ALPHA);
set(gca,'TickDir','out','FontSize',15)
xlabel('Z','FontSize',20)
ylabel('ALPHA','FontSize',20)

TRAV_VECTOR(900,1)
TRAV_VECTOR_ALPHA(900,1)
TRAV_VECTOR_Y(900,1)
```

```
%}
```

```
%PROGRAM NAME: 'HEAVISIDE_GOLDBETTER_PDE'
%This calling function contains the GOLDBETTER PDE system, discretised
%using the 'method of lines'.

function [dCONC_dt]=HEAVISIDE_GOLDBETTER_PDE(t,CONC,v_0,v_1,k,k_f,k_A,k_R,K_2,m,n,p,V_M2,V

x=linspace(0,fx,N);



%uncomment the code below for a piecewise profile which is held for all time.
BETA = HEAVISIDE(x);%note that B is outputted as a row vector. enter piecewise(x) for line
BETA = BETA(:);


%uncomment the code below for piecewise profile only held for an initial time.
%{
if (t>=0)&&(t<=1)
BETA = HEAVISIDE(x);%note that B is outputted as a row vector. enter piecewise(x) for line
BETA = BETA(:);

else
BETA = repmat(0.27,N,1);
end
%}

%{
if (t>=0)&&(t<=20)
BETA = HEAVISIDE(x);%note that B is outputted as a row vector. enter piecewise(x) for line
BETA = BETA(:);
    elseif (t>=25)&&(t<=26)
    BETA = HEAVISIDE(x);%note that B is outputted as a row vector. enter piecewise(x) for
    BETA = BETA(:);
else
BETA = repmat(0.27,N,1);
end
%}

DS=fx/N;

dCONC_dt=[((D1/(DS^2)).*(M*CONC(1:N))   +v_0   +v_1.*BETA-   V_M2.*((CONC(1:N).^n)./(((K_2
            ((D2/(DS^2)).*(M*CONC(N+1:2*N))  +V_M2.*((CONC(1:N).^n)./(((K_2)^n)+(CONC(1:N)
return

%************************************TESTING CODE
%enter these into command line to test if expression above is correct or
%not.

%v_0=1;v_1=7.3;k=10;k_f=1;k_A=0.9;k_R=2;K_2=1;m=2;n=2;p=4;V_M2=65;V_M3=500;BETA=0.301;D1=0
%x=linspace(0,fx,N);
```

```
%DS=fx/N;
%CONC=[0.1;0.1;0.1;1.35;1.35;1.35]
%dia1=[-2;repmat(-2,N-2,1);-2]; %the vector that is to be the main diagonal of the matrix.
%dia2=[2;repmat(1,N-2,1)];%the vector that is to be above the main diagonal.
%dia3=[repmat(1,N-2,1);2];%the vector that is to be below the main diagonal.
%M=diag(dia1,0)+diag(dia2,1)+diag(dia3,-1);%the spatial matrix.
```

```
%PROGRAM NAME: 'HEAVISIDE'
%This calling function contains the spatially varying piecewise profile of paramter BETA.
function y=HEAVISIDE(x)
fx=1000;
y(find(x<=0.65*fx))=0.27;
y(find((0.65*fx)<x & x<=(0.85)*fx))=0.30;
y(find((0.85)*fx<x))=0.27;

%*******************************************************
%type these into the command window to see the shape of the piecewise profile.
%{
fx=1000;
N=10000;
x=linspace(0,fx,N);
y=HEAVISIDE(x);
plot(x,y)
set(gca,'TickDir','out','FontSize',15)
ylim([0,1])
xlabel('axial distance (\mum)','FontSize',20)
ylabel('\beta proportion of IP_3 receptors activated','FontSize',20)
%}

%insert these for HEAVISIDE function appropriate for GOLDBETTER system.
%{
y(find(x<=0.25*fx))=0.27;
y(find((0.25*fx)<x & x<=(7/20)*fx))=0.50;
y(find((0.75)*fx<x))=0.27;
%}

%insert this for HEAVISIDE function appropriate for GOLDBETTER. but
%HEAVISTEP is more towards the upstream of axial distance. and one side of
%the step is elevated beyond agonist conc for oscillations. This is a more
%useful HEAVISIDE than the previous one.
%{
y(find(x<=0.65*fx))=0.27;
y(find((0.65*fx)<x & x<=(0.85)*fx))=0.50;
y(find((0.85)*fx<x))=0.9;
%}

%This HEAVISIDE has no upper elevated statdy state.
%{
y(find(x<=0.65*fx))=0.27;
y(find((0.65*fx)<x & x<=(0.85)*fx))=0.50;
y(find((0.85)*fx<x))=0.27;
%}

%This HEAVISIDE used for testing purposes.
%{
y(find(x<=0.65*fx))=0;
y(find((0.65*fx)<x & x<=(0.85)*fx))=0.77;
```

```
y(find((0.85)*fx<x))=0;
%}

%HEAVISIDE with no spatial variation.
%{
y(find(x<=0.65*fx))=0.27;
y(find((0.65*fx)<x & x<=(0.85)*fx))=0.27;
y(find((0.85)*fx<x))=0.27;
%}
```

```
%PROGRAM NAME: 'GOLDBETTER_TWFINAL2_RECOVER'
%code attempts to find the eigenvalues of the GOLDBETTER travelling wave
%system for a range of different values of c(wavespeed), for a specific fixed point.

%{
USER INPUT:
*ENTER RANGE OF C VALUES YOU WANT TO VARY OVER
*ENTER THE VALUE OF PARAMETER BETA.
*ENTER THE INITIAL GUESS OF THE FIXED POINT FOR THE SPECIFIC VALUE OF BETA.
%}

%system parameters
v_0=1;
v_1=7.3;
k=10;
k_f=1;
k_A=0.9;
k_R=2;
k_2=1;
m=2;
n=2;
p=4;
V_M2=65;
V_M3=500;
%USER INPUT
BETA=0.291;
%USER INPUT
c_FINAL=3; %define the range of c you want to vary over.
c_START=1;
c_NUMPOINTS=5000; %define the step sizes you want to vary c with.
c_STEP=(c_FINAL-c_START)/c_NUMPOINTS;

for INDEX=1:c_NUMPOINTS
f=@(a)[a(2);
(1/50)*(a(2)*(1+INDEX*c_STEP)-v_0-v_1*BETA+V_M2*(a(1))^n/(k_2^n+(a(1))^n)-V_M3*a(3)^m*a(1)
(V_M2*a(1)^n/(k_2^n+a(1)^n)-V_M3*a(3)^m*a(1)^p/((k_R^m+a(3)^m)*(k_A^p+a(1)^p))-k_f*a(3))/(
%opts = optimset('FinDiffType','central','Diagnostics','on');
%USER INPUT
[FIXEDPOINT,~,~,output,JACOBIAN] = fsolve(f, [0.3124300000;0;2.073245878]);
EIGENVALUES(:,INDEX)=eig(JACOBIAN,'nobalance');
end

%fixed point for BETA=0.291 is [0.3124300000;0;2.073245878]
%for BETA=0.27 is [0.2971;0;2.13996]

EIGENVALUES; %EIGNEVALUES contains the 4 eigenvalues of the system (rows) for various diff
REAL=real(EIGENVALUES); %REAL contains only the real parts of EIGENVALUES.
IMAGINARY=imag(EIGENVALUES); %IMAGINARY contains only the imaginary parts of EIGENVALUES.

REAL1=REAL(1,:);
```

```
REAL1=REAL1.'; %REAL1 contains only the first row of REAL.
REAL2=REAL(2,:);
REAL2=REAL2.'; %REAL2 contains only the first row of REAL.
REAL3=REAL(3,:);
REAL3=REAL3.'; %REAL3 contains only the first row of REAL.

IMAGINARY1=IMAGINARY(1,:);
IMAGINARY1=IMAGINARY1.'; %IMAGAINARY1 contains only the first row of IMAGINARY.
IMAGINARY2=IMAGINARY(2,:);
IMAGINARY2=IMAGINARY2.'; %IMAGAINARY2 contains only the first row of IMAGINARY.
IMAGINARY3=IMAGINARY(3,:);
IMAGINARY3=IMAGINARY3.'; %IMAGAINARY3 contains only the first row of IMAGINARY.

c_VALUES=linspace(c_START,c_FINAL,c_NUMPOINTS);%The range of values you want to vary param

FIXEDPOINT


plot3(REAL1,IMAGINARY1,c_VALUES,'b');
hold on
plot3(REAL2,IMAGINARY2,c_VALUES,'r');
hold on
plot3(REAL3,IMAGINARY3,c_VALUES,'c');
hold off
xlabel('REAL')
ylabel('IMAGINARY')
zlabel('c (wavespeed)')
grid on


%{
plot(REAL1,IMAGINARY1,'r');
hold on
plot(REAL2,IMAGINARY2,'b');
hold on
plot(REAL3,IMAGINARY3,'c');
hold off
xlabel('REAL')
ylabel('IMAGINARY')
grid on
%}
```

Bibliography

Agladze, K. I. and Krinsky, V. I. (**1982**): Multi-armed vortices in an active chemical medium, Nature, Vol. 296 pp. 424–426.

Arensbak, B.; Mikkelsen, H. B.; Gustafsson, F. and Christensen, T. (**2001**): Expression of connexin 37 , 40 , and 43 mRNA and protein in renal preglomerular arterioles pp. 479–487.

A.T., W. (**1974**): Rotating Chemical Reactions, Scientific American, Vol. 230, No. 6 pp. 82–95.

Atri, a.; Amundson, J.; Clapham, D. and Sneyd, J. (**1993**): A single-pool model for intracellular calcium oscillations and waves in the Xenopus laevis oocyte., Biophysical journal, Vol. 65, No. 4 pp. 1727–39.

Berridge, M. J. (**1993**): Inositol trisphosphate and calcium signalling., Nature, Vol. 361 pp. 315–325.

Caro, C.; Fitz-Gerald, J. and Shroter, J. (**1969**): Arterial Wall Shear and distribution of early atheroma in man, Nature pp. 1159–1161.

Carroll, M. (**1989**): Organelles, Guildford Press, New York.

Dai, G.; Kaazempur-Mofrad, M. R.; Natarajan, S.; Zhang, Y.; Vaughn, S.; Blackman, B. R.; Kamm, R. D.; García-Cardeña, G. and Gimbrone, M. A. (**2004**): Distinct endothelial phenotypes evoked by arterial waveforms derived from atherosclerosis-susceptible and -resistant regions of human vasculature., Proceedings of the National Academy of Sciences of the United States of America, Vol. 101 pp. 14871–14876.

Diep, H. K.; Vigmond, E. J.; Segal, S. S. and Welsh, D. G. (**2005**): Defining electrical communication in skeletal muscle resistance arteries: a computational approach., The Journal of physiology, Vol. 568, No. Pt 1 pp. 267–81.

Fall, C. P. (**2002**): Computational Cell Biology, Vol. 20.

Goldberg, G. S.; Valiunas, V. and Brink, P. R. (**2004**): Selective permeability of gap junction channels., Biochimica et biophysica acta, Vol. 1662 pp. 96–101.

Goldbeter, A.; Dupont, G. and Berridge, M. J. (**1990**): Minimal model for signal-induced Ca2+ oscillations and for their frequency encoding through protein phosphorylation., Proceedings of the National Academy of Sciences of the United States of America, Vol. 87 pp. 1461–1465.

Haefliger, J.-A.; Nicod, P. and Meda, P. (**2004**): Contribution of connexins to the function of the vascular wall., Cardiovascular Research, Vol. 62 pp. 345–356.

Hill, C. E.; Phillips, J. K. and Sandow, S. L. (**2001**): Heterogeneous control of blood flow amongst different vascular beds., Medicinal research reviews, Vol. 21, No. 1 pp. 1–60.

Johnstone, S.; Isakson, B. and Locke, D. (**2009**): Biological and biophysical properties of vascular connexin channels., International review of cell and molecular biology, Vol. 278 pp. 69–118.

Keener, J. and Sneyd, J. (**2009**): Mathematical Physiology I: Cellular Physiology, Vol. 8/1.

van Kempen, M. J. and Jongsma, H. J. (**1999**): Distribution of connexin37, connexin40 and connexin43 in the aorta and coronary artery of several mammals., Histochemistry and cell biology, Vol. 112, No. 6 pp. 479–86.

Koenigsberger, M.; Sauser, R.; Bény, J.-L. and Meister, J.-J. (**2005**): Role of the endothelium on arterial vasomotion., Biophysical journal, Vol. 88, No. 6 pp. 3845–54.

Koenigsberger, M.; Sauser, R.; Lamboley, M.; Bény, J.-L. and Meister, J.-J. (**2004**): Ca2+ dynamics in a population of smooth muscle cells: modeling the recruitment and synchronization., Biophysical journal, Vol. 87, No. 1 pp. 92–104.

Koenigsberger, M.; Seppey, D.; Bény, J.-L. and Meister, J.-J. (**2010**): Mechanisms of propagation of intercellular calcium waves in arterial smooth muscle cells., Biophysical journal, Vol. 99, No. 2 pp. 333–43.

Lodish, H.; Berk, A.; Matsudaira, P.; Kaiser, C. A.; Krieger, M.; Scott, M. P.; Zipursky, L. and Darnell, J. (**2008**): Molecular Cell Biology, Vol. 4.

M, S. and J, B. (**1974**): Optimum Topographical conditions for reverberating cortical spreading depression in rats., Jounal of Neurobiology, Vol. 5 pp. 107–118.

Ma, P.; Ku, D. N. and X, L. (**1997**): MASS TRANSFER BIFURCATION, Vol. 9290.

Maini, P. K. (**1995**): Travelling Waves in biology, chemistry ecology and medicine, FORMA, Vol. 10, No. 3 pp. 145–280.

Meyer, T. and Stryer, L. (**1988**): Molecular model for receptor-stimulated calcium spiking., Proceedings of the National Academy of Sciences of the United States of America, Vol. 85, No. 14 pp. 5051–5.

Meyer, T. and Stryer, L. (**1991**): Calcium spiking., Annual review of biophysics and biophysical chemistry, Vol. 20 pp. 153–74.

Müller, S. C.; Plesser, T. and Hess, B. (**1985**): The structure of the core of the spiral wave in the belousov-zhabotinskii reaction., Science, Vol. 230 pp. 661–663.

Murray J.D. (**1989**): Mathematical Biology, Springer-Verlag, 3 edition.

Parthimos, D.; Edwards, D. H. and Griffith, T. M. (**1999**): Minimal model of arterial chaos generated by coupled intracellular and membrane Ca2+ oscillators., The American journal of physiology, Vol. 277 pp. H1119–H1144.

P.C., N. (**1983**): Attraction and adhesion in the slime mold Dictyostelium, in **J.E., S.** (Ed.), Fungal Differentiation: A Contemporary Synthesis, Marcel Dekker, New York, pp. 43–71.

Physiol, A. J.; Physiol, C.; Burt, J. M.; Fletcher, A. M.; Steele, T. D.; Wu, Y.; Cottrell, G. T.; Kurjiaka, D. T.; Wu, Y. A. N. and Janis, M. (**2013**): Alteration of Cx43 : Cx40 expression ratio in A7r5 cells Alteration of Cx43 : Cx40 expression ratio in A7r5 cells.

Rackauskas, M.; Kreuzberg, M. M.; Pranevicius, M.; Willecke, K.; Verselis, V. K. and Bukauskas, F. F. (**2007**a): Gating properties of heterotypic gap junction channels formed of connexins 40, 43, and 45., Biophysical Journal, Vol. 92 pp. 1952–1965.

Rackauskas, M.; Verselis, V. K. and Bukauskas, F. F. (**2007**b): Permeability of homotypic and heterotypic gap junction channels formed of cardiac connexins mCx30.2, Cx40, Cx43, and Cx45., American journal of physiology. Heart and circulatory physiology, Vol. 293 pp. H1729–H1736.

Roose, T.; Chapman, S. J. and Maini, P. K. (**2006**): A mathematical model for simultaneous spatio-temporal dynamics of calcium and inositol 1,4,5-trisphosphate in Madin-Darby canine kidney epithelial cells., Bulletin of mathematical biology, Vol. 68, No. 8 pp. 2027–51.

Shaikh, M. A.; Wall, D. J. N. and David, T. (**2012**): Macro-scale phenomena of arterial coupled cells: a massively parallel simulation., Journal of the Royal Society, Interface / the Royal Society, Vol. 9, No. 70 pp. 972–87.

Turing, A. M. (**1952**): The Chemical Basis of Morphogenesis.

Wilkins, M. and Sneyd, J. (**1998**): Intercellular spiral waves of calcium., Journal of theoretical biology, Vol. 191, No. 3 pp. 299–308.